1 Linear summation of metabotropic postsynaptic potentials follows coactivation of neurogliaform
2 interneurons

3

4 *Attila Ozsvár[1], Gergely Komlósi[1], Gáspár Oláh[1], Judith Baka[1], Gábor Molnár[1], Gábor Tamás[1,2,*]*

5 [1] *MTA-SZTE Research Group for Cortical Microcircuits of the Hungarian Academy of Sciences,*
6 *Department of Physiology, Anatomy and Neuroscience, University of Szeged, 52 Közép fasor, Szeged*
7 *6726, Hungary*

8 [2] *Lead Contact*

9 * Correspondence: gtamas@bio.u-szeged.hu (G.T.)

10

Summary

12

13 Summation of ionotropic receptor-mediated responses is critical in neuronal computation by shaping
14 input-output characteristics of neurons. However, arithmetics of summation for metabotropic signals
15 are not known. We characterized the combined ionotropic and metabotropic output of neocortical
16 neurogliaform cells (NGFCs) using electrophysiological and anatomical methods. These experiments
17 revealed that GABA receptors are activated up to 1.8 microns from release sites and confirmed
18 coactivation of putative NGFCs in superficial cortical layers in vivo. Triple recordings from presynaptic
19 NGFCs converging to a postsynaptic neuron revealed sublinear summation of ionotropic $GABA_A$
20 responses and linear summation of metabotropic $GABA_B$ responses. Based on a model combining
21 distances of volume transmission from release sites and distributions of all NGFC axon terminals, we
22 postulate that 2 to 3 NGFCs provide input to a point in the neuropil. We suggest that interactions of
23 metabotropic GABAergic responses remain linear even if most superficial layer interneurons
24 specialized to recruit $GABA_B$ receptors are simultaneously active.

25 Keywords: synaptic integration, neurogliaform cell, layer 1, neocortex, metabotropic $GABA_B$ receptor

26

Introduction

28

29 Each neuron in the cerebral cortex receives thousands of excitatory synaptic inputs that drive action
30 potential output. The efficacy and timing of excitation is effectively governed by GABAergic inhibitory
31 inputs that arrive with spatiotemporal precision onto different subcellular domains. Synchronization
32 of GABAergic inputs appears to be crucial in structuring cellular and network excitation and
33 behaviorally relevant rhythmic population activity (Klausberger & Somogyi, 2008). Diverse
34 subpopulations of GABAergic neurons contribute to network mechanisms at different temporal
35 windows and synchronized cells of particular interneuron types appear to fire in a stereotyped fashion
36 (Klausberger & Somogyi, 2008). In general, this frequently results in coactivation of similar (and
37 asynchronization of dissimilar) GABAergic inputs arriving to target neurons (Jang et al., 2020; Karnani
38 et al., 2016; Kvitsiani et al., 2013), that leads to postsynaptic summation of GABAergic responses
39 synchronously activated by presynaptic cells of the same type. Most GABAergic cell types exert
40 inhibitory control through ionotropic $GABA_A$ receptors allowing Cl^- ions to pass rapidly through the

41 membrane (Barker, Ransom, & Neurobiology, 2009) and depending on the magnitude of GABA release
42 and/or the number of synchronously active presynaptic interneurons, synaptic and extrasynaptic
43 GABA$_A$ receptors could be recruited. The integration of ionotropic inhibitory signals on the surface of
44 target cell dendrites is temporally precise and spatially specific (Bloss et al., 2016; Klausberger, 2009;
45 Müller, Beck, Coulter, & Remy, 2012). Summation of ionotropic receptor-mediated responses are
46 extensively studied in the neocortex and predominantly characterized by nonlinear rules of interaction
47 (Jadi, Polsky, Schiller, & Mel, 2012; Koch, Poggio, & Torre, 1983; London & Häusser, 2005; Qian &
48 Sejnowski, 1990; Silver, 2010). In addition to GABA$_A$ receptors, metabotropic GABA$_B$ receptor
49 activation can occur during synchronized and/or long lasting activation of GABAergic inputs (Dutar &
50 Nicoll, 1988; Isaacson, Solis, & Nicoll, 1993; Mody, De Koninck, Otis, & Soltesz, 1994; Scanziani, 2000;
51 Thomson & Destexhe, 1999). Among the various interneuron subtypes identified in the neocortex
52 (Ascoli et al., 2008; Markram et al., 2004; Schuman et al., 2019), only NGFCs are known to be especially
53 effective in recruiting metabotropic GABA$_B$ receptors in addition to ionotropic GABA$_A$ receptors by
54 sporadic firing using single cell triggered volume transmission in the microcircuit (Oláh et al., 2009;
55 Tamas, 2003). GABA binding to GABA$_B$ receptors catalyzes GDP/GTP exchange at the Gα subunit and
56 the separation of Gβγ (Bettler, Kaupmann, Mosbacher, & Gassmann, 2004). The Gβγ subunits - as
57 membrane-anchored proteins - locally diffuse in the plasma membrane and up to four Gβγ subunits
58 bind cooperatively to G-protein gated inward rectifier (GIRK) channels and trigger a channel opening
59 that drives the membrane potential towards the K$^+$ reverse potential (Dascal, 1997; Inanobe & Kurachi,
60 2014; Stanfield, Nakajima, & Nakajima, 2002; Wang, Touhara, Weir, Bean, & MacKinnon, 2016;
61 Wickman & Clapham, 1995). Activation of GABA$_B$ receptors by NGFCs control the firing of dendritic
62 spikes in the distal dendritic domain in pyramidal cells (PCs) (Larkum, Kaiser, & Sakmann, 2002; L. M.
63 Palmer et al., 2012; Wozny & Williams, 2011) and activity in the prefrontal cortex is effectively
64 controlled by the strong feed-forward GABA$_B$ inhibition mediated by NGFCs (Jackson, Karnani,
65 Zemelman, Burdakov, & Lee, 2018). Moreover, GABA$_B$ receptors contribute to termination of
66 persistent cortical activity (Craig, Mayne, Bettler, Paulsen, & McBain, 2013) and slow inhibition
67 contributes to theta oscillations in the hippocampus (Capogna & Pearce, 2011). Relative to the
68 summation of ionotropic responses, postsynaptic summation properties of metabotropic receptors
69 are unexplored and to date, there has been no experimental analysis of how neurons integrate electric
70 signals that are linked to inhibitory metabotropic receptors. We set out to test the summation of
71 metabotropic receptor-mediated postsynaptic responses by direct measurements of convergent
72 inputs arriving from simultaneously active NGFCs and to characterize the likelihood and arithmetics of
73 metabotropic receptor interactions in a model of population output by incorporating experimentally
74 determined functional and structural synaptic properties of NGFCs.
75

76 **Results**

77 **Quantal and structural characteristics of GABAergic connections established by individual**
78 **neurogliaform cells**

79 NGFCs are capable of activating postsynaptic receptors in the vicinity of their presynaptic boutons via
80 volume transmission (Oláh et al., 2009). To gain insight into the possible effective radius of volume
81 transmission we characterized properties of NGFC-PC connections. *In vitro* simultaneous dual whole-
82 cell patch clamp recordings were carried out on synaptically connected L1 NGFC to L2/3 PC pairs in
83 brain slices from the somatosensory cortex of juvenile male Wistar rats. Pre- and postsynaptic cells
84 were chosen based on their characteristic passive membrane and firing properties (Fig. 1A) and
85 recorded neurons were filled with biocytin, allowing *post hoc* anatomical reconstruction of recorded
86 cells and estimation of putative synaptic release sites (Fig. 1B, H). Single action potentials triggered in
87 NGFCs elicit biphasic GABA$_A$ and GABA$_B$ receptor-mediated responses on the target neurons (Tamas,
88 2003). To determine the number of functional release sites, we recorded IPSCs under different release
89 probability by varying extracellular Ca^{2+} and Mg^{2+} concentrations (Fig. 1C, F). NGFC evoked inhibitory

90   postsynaptic potentials show robust use-dependent synaptic depression, therefore we limited the
91   intervals of action potential triggered in NGFCs to 1 minute (Karayannis et al., 2010; Tamas, 2003). We
92   collected a dataset of n= 8 NGFC to PC pairs with an average of 65.5 ± 5.264 trials per pair and 32.75 ±
93   4.155 trials for a given Mg^{2+}/Ca^{2+} concentration per conditions. The limited number of trials due to the
94   use-dependent synaptic depression of NGFCs restricted our approach to Bayesian Quantal Analysis
95   (BQA) previously shown to be robust for the estimation of quantal parameters (Bhumbra & Beato,
96   2013a). As expected, IPSC peak amplitudes were modulated by elevated (3 mM) and reduced (1.5 mM
97   or 2 mM) extracellular Ca^{2+} concentrations consistent with the decline in release probability (Fig. 1D).
98   Distributions of IPSC amplitudes detected in paired recordings were in good agreement with the
99   estimated quantal amplitude distribution derived from the BQA (Fig. 1E). According to BQA, the
100 estimated mean number of functional release sites (Nfrs) was 10.96 ± 8.1 with a mean quantal size (q)
101 of 3.93 ± 1.21 pA (Fig. 1G). Full reconstruction of functionally connected NGFC-PC pairs (n= 6) allowed
102 comparisons of the Nfrs estimated by BQA and the number of putative release sites by counting the
103 number of presynaptic boutons located within increasing radial distances measured from postsynaptic
104 dendrites (Fig. 1H). Previous experiments showed that direct synaptic junctions are not required for
105 functional NGFC to PC connections (Oláh et al., 2009) and GABA reaches receptors up to 3 μm from
106 the release site (Farrant & Nusser, 2005; Overstreet-Wadiche & McBain, 2015; Overstreet, Jones, &
107 Westbrook, 2000). In agreement with earlier observations (Oláh et al., 2009), direct appositions were
108 not observed in most NGFC to PC pairs and the number of NGFC axonal boutons potentially involved
109 in eliciting postsynaptic responses increased by systematically increasing the radial distance from the
110 dendrites of PCs. Projecting the range of BQA-derived Nfrs estimates over the number of NGFC
111 boutons putatively involved in transmission for the same connections (Fig. 1H, red lines) suggests an
112 effective range of 0.86 to 1.75 μm for nonsynaptic volume transmission from NGFCs to PCs supporting
113 previous reports on distances covered by extrasynaptic GABAergic communication (Farrant & Nusser,
114 2005; Overstreet-Wadiche & McBain, 2015; Overstreet et al., 2000). Moreover, we detected linear
115 correlation (r= 0.863, p= 0.027) between BQA-derived Nfrs and the number of NGFC boutons putatively
116 involved in transmission at radial distances <1.5 μm from PC dendrites; decreasing or increasing the
117 distance resulted in the loss of correlation (Fig. 1I).

118

119 **Structural characteristics of GABAergic connections established by the population of layer 1**
120 **neurogliaform cells**

121 To have a better idea about how does the volume transmission radius potentially affect the fraction of
122 converging outputs of L1 NGFC population to the same space, we developed a model to assess the
123 overall output of NGFCs located in the supragranular layers of the neocortex. Unitary volume
124 transmission by NGFCs is limited to their extremely dense axonal arborization (Oláh et al., 2009; Rózsa
125 et al., 2017) Therefore, we determined the three-dimensional distribution of axon lengths of individual
126 NGFCs with Sholl analysis (Fig. 2A). By superimposing individual NGFC reconstructions centered by
127 their somata (n= 16; Fig. 2C) a representative distribution of axons was calculated as a function of
128 distance from the soma Fig. 2D). We also assessed the distance between axonal boutons (n= 1456)
129 along reconstructed axons of NGFCs (n= 6) and found that interbouton distances were 3.36 ± 2.54 μm
130 (Supplementary Fig. 1). Next, we developed an algorithm that generates model NGFCs (n= 52) by
131 growing axon arborizations similar (p= 0.99, two-sided K-S test, Fig. 2D) to the population of the
132 experimentally reconstructed representative distribution of NGFC axons (n= 16) using interactions of
133 segment lengths, branch point locations and segment orientations while keeping the density of axonal
134 boutons along axon segments (Fig. 2B, C). In order to achieve a relatively complete representation of
135 all NGFC axon terminals in a model at the populationlevel, we performed immunhistochemical
136 labelling of α-actinin2, which is known to label the overwhelming majority of supragranular NGFCs in

137 the neocortex (Uematsu et al., 2008). Somata immunoreactive for α-actinin2 in superficial cortical
138 layers showed distribution along the axis perpendicular to the surface of the cortex with a peak at ~50-
139 150 μm distance from the pia mater (Fig. 2E). According to this radial distribution and with no apparent
140 tendency along the horizontal axis we placed NGFC somatas in a 354 x 354 x 140 μm volume to create
141 a realistic spatial model of L1 NGFC population (Fig. 2F). Three dimensional pairwise shortest distances
142 between α-actinin2+ somata (n= 152) and distances between somata placed into the model space (n=
143 374) were similar (p= 0.51, two-sided K-S test, Fig. 2G). We then used the axon growing algorithm
144 detailed above from each soma position to model a population-wide distribution of NGFC axonal
145 release sites. Quantal and structural properties of NGFC to PC connections shown above suggest a
146 volume transmission distance of ~1.5 μm from potential sites of release (Fig. 1H, I), thus we mapped
147 the coverage of surrounding tissue with GABA simultaneously originating from all NGFC terminals with
148 a 1.5 μm of transmitter diffusion in the model. Using these conditions in simulations (n= 36), less than
149 8 NGFC axonal terminals contributed as effective GABA sources at any location in the superficial
150 neocortex (Fig. 2H). Moreover, these boutons originated from a limited number of presynaptic NGFCs;
151 when considering the extreme case of population-level cooperativity, i.e. when all putative NGFCs
152 were active, most frequently a single NGFC release site serve as a GABA source (67.7 ± 7%) and
153 potential interactions between two, three or more different NGFCs take place in limited occasions
154 (15.34 ± 2.1%, 8.5 ± 2.6% and 8.45 ± 3.16%, respectively). The outcome of these simulations is
155 consistent with earlier results suggesting that single cell driven volume transmission covers only the
156 close proximity of NGFCs (Oláh et al., 2009) but also indicates potential interactions between a
157 restricted number of neighbouring NGFCs.

158

159 **Coactivation of putative neurogliaform cells in L1 somatosensory cortex *in vivo***

160 Transcallosal fibers establish interhemispheric inhibition that operates via GABA$_B$ receptor activation
161 located on apical dendrites (L. M. Palmer et al., 2012) and it has been suggested that this massive
162 GABA$_B$ receptor recruitment in the superficial layers includes the activation of NGFCs (L. Palmer,
163 Murayama, & Larkum, 2012). To assess the fraction of synchronously active putative NGFCs under
164 close to physiological conditions, we applied *in vivo* two-photon Ca^{2+} imaging. We monitored the
165 activity of L1 neurons bulk-loaded with calcium indicator Oregon Green BAPTA-1-AM (OGB-1-AM) (Fig.
166 3A) during hindlimb stimulation, which results in the activation of transcallosal inputs in L1 of the
167 somatosensory cortex of urethane-anaesthetized rats (n= 6). Stimulation of the ipsilateral hindlimb
168 (200 mA, 10ms) evoked Ca^{2+} signals in a subpopulation of neurons in L1 (n= 114 neurons; n= 46 vs. 68
169 responsive vs. non-responsive neurons, respectively; data pooled from six animals; Fig. 3B, 3C). On
170 average 38.2 ± 5.2% of the L1 neurons were active following ipsilateral hindlimb stimulation, which is
171 remarkably similar to the proportion found earlier (L. M. Palmer et al., 2012) (Fig. 3E). To further
172 identify L1 neurons active during hindlimb stimulation, we performed immunohistochemistry for the
173 actin-binding protein α-actinin2, (Uematsu et al., 2008) (Fig. 3F) using the same cortical area of L1 on
174 which two-photon imaging was performed previously. Cross examination of neurons responsive/non-
175 responsive to hindlimb stimulation versus neurons immunopositive/negative for α-actinin2 revealed
176 that the majority of the active neurons were α-actinin2 positive (10 out of 15 neurons, 67%, n= 2
177 animals) and the majority of inactive neurons were α-actinin2 negative (22 out of 26 neurons, 85%,
178 Fig. 3G) suggesting that a substantial fraction of L1 NGFCs are activated during hindlimb stimulation.

179

180 **Summation of convergent, unitary IPSPs elicited by NGFC**

181 Our *in vivo* measurements above corroborate earlier results (L. M. Palmer et al., 2012) on widespread
182 simultaneous activation of putative L1 NGFCs in response to transcallosal inputs. To directly measure
183 the summation of converging inputs from superficial NGFCs, *in vitro* simultaneous triple recordings
184 were performed from two presynaptic NGFCs and a target PC (n= 4, Fig. 4A). First we measured the
185 amplitude of unitary IPSPs (n= 8) elicited by single NGFCs in the target PC and found that smaller and
186 bigger inputs in a triplet were -1.68 ± 1.51 mV and -2.19 ± 1.33 mV, respectively. Next we activated the
187 two NGFC inputs synchronously (0.17 ± 0.05 ms) and such coactivation resulted in moderately
188 sublinear summation of convergent IPSPs (maximal nonlinearity, -9.1 ± 4.3 %) measured as the
189 difference of calculated (-3.81 ± 2.76 mV) and experimentally determined (-3.57 ± 2.55 mV) sums of
190 convergent single inputs (n= 4; Fig. 4B). These results are in line with experiments showing moderately
191 sublinear interactions between identified, single cell evoked fast IPSPs (Tamás, Szabadics, & Somogyi,
192 2002). Interestingly, the time course of sublinearity followed the fast, presumably $GABA_A$ receptor-
193 mediated part of the unitary and summated IPSPs (Fig. 4C) suggesting that ionotropic and
194 metabotropic GABAergic components of the same input combinations might follow different rules of
195 summation. To test the interaction of unitary $GABA_B$ receptor-mediated IPSPs directly, we repeated
196 the experiments above with the application of the $GABA_A$ receptor antagonist gabazine (10 µM).
197 Pharmacological experiments on the output of NGFCs are very challenging due to the extreme
198 sensitivity of NGFC triggered IPSPs to presynaptic firing frequency (Capogna, 2011; Tamás,
199 Simon Anna, & Szabadics, 2003) forcing us to collect the data in a different set of triple recordings (n=
200 8, Fig. 4D). As expected (Tamás et al., 2003) unitary, gabazine insensitive, slow IPSPs had onset
201 latencies, rise times and half-widths similar to $GABA_B$ receptor-mediated responses (49.42 ± 5.8 ms,
202 86.95 ± 8.82 ms, and 252.27 ± 36.92 ms, respectively, n= 16, Fig. 4E). Peak amplitudes of converging
203 smaller and bigger slow IPSPs were -0.66±0.22 mV and -0.94±0.37 mV respectively. Synchronous
204 activation of two presynaptic NGFC converging onto the same pyramidal cell resulted in linear (-1.6 ±
205 6.6%) summation of slow IPSPs as peak amplitudes of calculated sums of individual inputs versus
206 experimentally recorded compound responses were -1.58 ± 0.53 mV and -1.60 ± 0.55 mV, respectively
207 (Fig. 4F). Taken together, our triple recordings in gabazine versus control conditions suggest linear
208 interactions between slow, $GABA_B$ IPSPs as opposed to sublinearly summating fast, $GABA_A$ IPSPs
209 elicited by the same presynaptic interneuron population.

210

211 **Integration of $GABA_B$ receptor-mediated responses are not affected by HCN channel and GABA**
212 **reuptake**

213 The predominant target area of the superficial NGFCs, the distal apical dendritic membrane of PCs,
214 express voltage-dependent hyperpolarization-activated cyclic nucleotide-gated channel 1 (HCN1)
215 known to attenuate dendritic signals (Berger, Larkum, & Lüscher, 2001; Kalmbach et al., 2018; Lörincz,
216 Notomi, Tamás, Shigemoto, & Nusser, 2002; Robinson & Siegelbaum, 2003; Sheets et al., 2011). To
217 investigate whether HCN1 channels contribute to mechanisms of interactions between $GABA_B$
218 receptor-mediated postsynaptic responses we performed experiments on NGFC-to-PC pairs and
219 evoked 1 to 4 action potentials (APs) in a single presynaptic NGFC at 100 Hz. This experimental
220 configuration mimics the extreme conditions when multiple presynaptic release sites converge in a
221 tight space and creating excessive GABAB receptor mediated inhibition. (Fig 5A). Triggering a single
222 spike in the presence of gabazine (10 µM) did not saturate postsynaptic $GABA_B$ receptors since the
223 postsynaptic response induced by two spikes was proportional to the arithmetic sum of unitary
224 postsynaptic responses (experimental sums: -1.25 mV calculated sums: -1.26 mV), apparently showing
225 linear summation properties similar to triple recordings testing summation convergent inputs above.
226 However, further increase in the number of evoked APs to 3 and 4 introduced sublinearity to
227 summation (n= 6, 1AP: -0.63 ± 0.50 mV, 2APs: -1.25 ± 1.06 mV, 3APs: -1.53 ± 0.84 mV, 4APs: -1.61 ±

228 1.09 mV, Fig. 5B; normalized values: 2APs: 2.00 ± 1.08, 3APs: 2.34 ± 1.16, 4APs: 3.17 ± 1.26, Fig. 5C).
229 Importantly, recordings in the presence of HCN1 channel blocker, ZD-2788 (10 µm) showed summation
230 properties similar to control, summation was linear with two APs and changed to slightly sublinear
231 upon the 3rd to 4th spike, (n= 5, 1AP: -0.82 ± 0.63 mV, 2APs: -1.59 ± 0.76 mV, 3APs: -1.66 ± 0.72 mV,
232 4APs: -1.90 ± 1.07 mV, Fig. 5B; normalized values and its comparison to control: 2APs: 2.06 ± 1.06, p=
233 0.983; 3APs: 1.99 ± 1.17, p= 0.362; 4APs: 2.56 ± 1.6, p= 0.336; two-sided MW U test, Fig. 5C). These
234 experiments suggest that when a physiologically probable number of NGFCs are simultaneously active,
235 HCN1 channels are locally not recruited to interfere with the summation of $GABA_B$ receptor-mediated
236 responses.

237 Previous experiments suggested that a single AP in a NGFC is able to fill the surrounding extracellular
238 space with an effective concentration of GABA (Oláh et al., 2009) and, in turn, extracellular GABA
239 concentration producing $GABA_B$ receptor activation is tightly regulated via GABA transporters (GAT-1)
240 (Gonzalez-Burgos, Rotaru, Zaitsev, Povysheva, & Lewis, 2009; Isaacson et al., 1993; Rózsa et al., 2017;
241 Szabadics, Tamas, & Soltesz, 2007). Therefore, we tested whether GAT-1 activity affects the
242 summation of $GABA_B$ receptor-mediated responses potentially limiting the number of $GABA_B$ receptors
243 reached by GABA released by NGFCs. Selective blockade of GAT-1 with NO-711 (10 µm) increased the
244 amplitude of $GABA_B$ receptor-mediated IPSP, however, it did not influence summation properties (n=
245 6, 1AP: -1.11 ± 0.62 mV, 2APs: -2.28 ± 1.07 mV, 3APs: -3.1 ± 0.40 mV, 4APs: -3.54 ± 1.59 mV, Fig. 5B;
246 normalized values and its comparison to control: 2APs: 2.06 ± 1.17, p= 0.853; 3APs: 2.36 ± 0.31, p=
247 0.645; 4APs: 2.97 ± 1.54, p= 0.515; two-sided MW U test, Fig. 5C). Accordingly, interactions between
248 an *in vivo* realistic number of simultaneously active NGFCs lead to linear $GABA_B$ response summation
249 even if increased concentration of GABA is present in the extracellular space.

250

Subcellular localization of $GABA_B$ receptor-GIRK channel complex determines summation
properties

253 High resolution quantitative electron microscopy showed that $GABA_B$ receptors and GIRK channels are
254 segregated on dendritic shafts, however, receptor-channel complexes colocalize on dendritic spines
255 (Á. Kulik et al., 2006). Theoretical studies suggest that the distance between the receptor and effector
256 limits the recruitment of effector molecules to the vicinity of receptors (Brinkerhoff, Choi, &
257 Linderman, 2008; Á. Kulik et al., 2006), thus we asked if linear summation was potentially a result of
258 the locally constrained $GABA_B$ receptor - GIRK channel interaction when several presynaptic inputs
259 converge. To this end, we constructed a simulation environment based on a previously published
260 three-dimensional reconstruction of a postsynaptic dendritic segment (Edwards et al., 2014) targeted
261 by realistically positioned release sites of NGFCs (Fig. 6A). Molecular interactions in this spatially
262 realistic system were modeled using Monte Carlo algorithms to simulate movements and reactions of
263 molecules (Kerr et al., 2008). Membranes of the postsynaptic dendritic segment were populated (see
264 methods) with $GABA_B$ receptors and GIRK channels according to compartment-dependent data from
265 SDS-digested freeze-fracture replica immunolabeling (Á. Kulik et al., 2006) (Fig. 6C). Neurotransmitter
266 diffusion in the brain is influenced by tissue tortuosity and the fraction of extracellular space in total
267 tissue volume (Sykova & Nicholson, 2008), thus we simulated realistic molecular diffusion in tortuous
268 extracellular space (Tao, Tao, & Nicholson, 2005) (see methods). The number and position of NGFC
269 presynaptic boutons around the postsynaptic dendritic segments in the model were used according to
270 structural characteristics of GABAergic connections established by individual NGFCs (n= 4 boutons 1.2
271 ± 0.7 µm from the dendrite; Fig. 1I, H) and according to the bouton density determined for the overall
272 output of NGFC population (Fig. 2F). Previous work suggests that a single AP in a NGFC generates GABA
273 concentrations of 1 to 60 µM lasting for 20-200 ms (Karayannis et al., 2010) so we used a similar ~1 to

274 60 µM of GABA concentration range at 0.5 to 2 µm distance from the release sites (Supplementary Fig.
275 4) and GABA exposure times of 114.87 ± 2.1 ms with decay time constants of 11.52 ± 0.14 ms. Our
276 modeling trials show that single AP triggered GABA release can activate a total of 5.82 ± 2.43 GABA$_B$
277 receptors (2.81 ± 1.55 on spine, 3.01 ± 1.71 on the shaft). Furthermore, activation of GABA$_B$ receptors
278 triggers intracellular mechanisms and the initial GDP/GTP exchange at the Gα subunit separates the G-
279 protein heterotrimeric protein and produces Gβγ subunits (peak number of Gβγ subunits for single AP:
280 338.54 ± 138.75). Lateral membrane diffusion of Gβγ subunits lead to the activation of 3.66 ± 2.17 GIRK
281 channels in total (2.47 ± 1.88 on spine, 1.17 ± 1.26 on the shaft) in response to single AP. Next,
282 consecutive GABA releases were induced with 10 ms delays to replicate the 100 Hz stimulation
283 protocol used in the experiments above (Fig. 5A). The increased GABA concentration from two
284 sequential stimuli raised the number of active GABA$_B$ receptors to 11.29 ± 3.48 (5.57 ± 2.36 on spine,
285 5.72 ± 2.52 on the shaft). Three and four consecutive releases activated a total of 16.19 ± 3.88 and
286 20.99 ± 4.99 GABA$_B$ receptors, respectively (7.96 ± 2.74 on spine, 8.23 ± 2.97 on the shaft and 10.62 ±
287 3.28 on spine, 10.37 ± 3.53 on the shaft, respectively). When modeling consecutive GABA releases,
288 massive amount of Gβγ subunits were produced together with a decline in relative production efficacy
289 per APs, possibly due to the limited number of G-proteins serving as a substrate in the vicinity of active
290 receptor clusters (peak number of Gβγ subunits for 2AP: 612.10 ± 171.95; 3AP: 857.78±194.14; 4AP:
291 1081.81 ± 229.57). Two consecutive APs resulted in the activation of 6.98 ± 3.29 GIRK channels (2.13
292 ± 1.63 on dendritic shaft and 4.85 ± 2.65 on spine) in the simulations. Importantly, this number of
293 activated GIRK channels in response to two APs was close to the arithmetic sum of the number of GIRK
294 channels activated by two single AP responses (-4.87% in total, -1.86% on spines and -9.86% on the
295 shaft; Fig. 4E,5A). Further increase in the GABA exposure proportional to three and four action
296 potentials lead to the activation of 10.39 and 12.89 GIRK channels, respectively (7.01 ± 3.11 and 8.68
297 ± 3.46 on spines and 3.37 ± 2.08 and 4.21 ±2. 48 on the shaft, respectively). These numbers of GIRK
298 channels corresponded to -5.68 and -13.58% of the arithmetic sum of GIRK channels activated by three
299 and four single AP responses (-5.71 and 13.82% on spines and -4.15 and -11.16% on the shaft).

300 GABA$_B$ receptor and GIRK channel complexes located in particular subcellular compartments appeared
301 to have different effectiveness of recruiting GABA$_B$ receptors and active GIRK channels in our
302 simulations (Fig. 6D). We observed different numbers of GABA$_B$ receptors activated on the shaft and
303 spine (Normalized values to 1AP: 2APs: shaft: 1.91 ± 0.84, spine: 1.98 ± 0.84, n= 534, p= 0.009; 3APs:
304 shaft: 2.74 ± 0.99, spine: 2.84 ± 0.98, n= 1871, p= 0.173; 3APs: shaft: 3.45 ± 1.18, spine: 3.78 ± 1.17, n=
305 709, p< 0.005, two-sided MW U test, Fig. 6E). The recruitment of GIRK channels was more effective on
306 spines compared to shafts when triggering 2 APs (Normalized values to 1AP: shaft: 1.8±1.37, spine:
307 1.96±1.07, n=534, p<0.005); the trend was similar in response to three and four APs, but results were
308 not significant (Normalized values to 1AP: 3AP: shaft: 2.84±1.75, spine: 2.84 ± 1.26, n= 1871, p= 0.109;
309 4AP: shaft: 3.55 ± 2.09, spine: 3.52 ± 1.4, n= 709, p= 0.216, two-sided MW U test, Fig. 6E). The
310 compartment-specific effectiveness of signaling as the ratio of activated GIRK channels and active
311 GABA$_B$ receptors (Fig. 6F) shows that spines represent the preferred site of action corroborating earlier
312 suggestions (Qian & Sejnowski, 1990).

313

Discussion

315 The unique inhibitory communication via volume transmission separates NGFC interneurons from
316 other interneuron classes in the neocortex. Numerous observations support the idea of volume
317 transmission (Overstreet-Wadiche & McBain, 2015). (1) NGFC activation generates an unusually
318 prolonged inhibition on the postsynaptic cell (Karayannis et al., 2010; Mańko, Bienvenu, Dalezios, &
319 Capogna, 2012; Oláh et al., 2009; Szabadics et al., 2007). (2) Released GABA acts on synaptic and

320 extrasynaptic GABA receptors (Karayannis et al., 2010; Oláh et al., 2009; Price, 2005; Tamas, 2003), (3)
321 as well as on nearby presynaptic terminals (Oláh et al., 2009). (4) NGFCs show a very high rate of
322 functional coupling between the neighboring neurons (Jiang et al., 2015; Oláh et al., 2009). (5)
323 Ultrastructural observations showed the lack of clearly defined postsynaptic elements in the
324 apposition of the NGFC boutons (Mańko et al., 2012; Oláh et al., 2009; Vida, Halasy, Szinyei, Somogyi,
325 & Buhl, 1998). (6) NGFCs act on astrocytes within the reach of their axonal arborization through
326 nonsynaptic coupling (Rózsa et al., 2017). The distance of effective operation through NGFC driven
327 volume transmission, however, is not clear. Here, we used functional and structural characterization
328 of NGFC-PC inhibitory connections and suggest that GABA released from NGFC axonal terminals
329 activates GABA receptors up to about ~1.8 µm, a result remarkably similar to previous estimations for
330 the range of extrasynaptic action of synaptically released GABA (Farrant & Nusser, 2005; Overstreet-
331 Wadiche & McBain, 2015; Overstreet et al., 2000) Our experiments also shed light to some quantal
332 properties of NGFC's GABA release. These experiments are constrained by the robust use-dependent
333 depression mediated by NGFCs (Karayannis et al., 2010; Tamás et al., 2003), therefore implementation
334 of multiple probability fluctuation analysis (MPFA) (Silver, 2003), the gold standard for quantal analysis,
335 was not feasible and BQA (Bhumbra & Beato, 2013b) was needed as an alternative. The revealed linear
336 correlation between BQA-derived Nfrs and the number of NGFC boutons putatively involved in
337 transmission is compatible with the release of a single docked vesicle from individual NGFC boutons
338 and suggest that multivesicular release is not essential for GABAergic volume transmission.

339 The functional distance of volume transmission is particularly important for the characterization of
340 interactions between NGFCs and for understanding the population output of NGFCs. Realistic
341 representation of an entire subpopulation of neurons is considered essential for the interpretation of
342 network functions (Karnani, Agetsuma, & Yuste, 2014; Markram et al., 2015) and pioneering full-scale
343 data-driven models were effective in deciphering emerging functions of interneuron populations
344 (Bezaire, Raikov, Burk, Vyas, & Soltesz, 2016). However, network diagrams addressing the function of
345 NGFCs exclusively based on synaptic connectivity underestimate the spread of output without
346 incorporating volume transmission by an order of magnitude (Oláh et al., 2009). Although the concept
347 of blanket inhibition has been suggested for networks of interneurons populations having overlapping
348 axonal arborizations and dense synaptic output (Karnani et al., 2014), our spatial model based on high
349 resolution reconstructions of labeled NGFCs takes the concept to its extremes and reveals an
350 unprecedented density of release sites for a population of cortical neuron and shows that the
351 overwhelming majority of the superficial cortical space is effectively covered by at least one NGFC. At
352 the same time, the redundancy of the NGFC population is limited and a single cortical spatial voxel is
353 reached by GABA released from a limited number of individual NGFCs, ~83 % of space is covered by 1
354 or 2 NGFCs. Our relatively simple *in vivo* approach to gauge potential synchronous action of NGFCs
355 gave positive results. This is in line with earlier observations suggesting widespread action of putative
356 NGFCs in terminating persistent activity (Craig et al., 2013), or powerfully suppressing dendritic Ca^{2+}
357 dynamics in L2/3 and L/5 (L. M. Palmer et al., 2012; Wozny & Williams, 2011). Strong cholinergic
358 neuromodulation of NGFCs (Poorthuis et al., 2018) and frequent gap junctional coupling between
359 NGFCs (Simon, Oláh, Molnár, Szabadics, & Tamás, 2005) further facilitates concerted action and are
360 likely to play a major role in synchronizing the NGFC network (Yao et al., 2016).

361 When studying simultaneous action of NGFCs, our direct measurements of two converging NGFC
362 inputs on L2/3 PC from simultaneous triple whole cell patch clamp recordings revealed sublinear
363 summation properties for ionotropic $GABA_A$ receptor mediated responses. These results support
364 classic theories on synaptic input interactions (Jadi et al., 2012; Koch et al., 1983; London & Häusser,
365 2005; Qian & Sejnowski, 1990; Silver, 2010) and are in line with earlier experiments measuring
366 interactions of anatomically identified inputs converging to neighboring areas of the dendritic tree of

367　the same postsynaptic cell (Hao, Wang, Dan, Poo, & Zhang, 2009; Tamás et al., 2002). Mechanisms of
368　interaction between convergent inputs from NGFCs might be similar to those suggested for short-term
369　synaptic depression of GABA$_A$ responses such as local drops in Cl$^-$ driving force and membrane
370　conductance (Huguenard & Alger, 1986; McCarren & Alger, 1985; Staley & Proctor, 1999). To our
371　knowledge, the simultaneous triple recordings of two presynaptic NGFCs targeting the same
372　postsynaptic PC represent the first direct experimental attempt addressing the summation of
373　metabotropic receptor mediated postsynaptic interactions. To date, scarce computational model
374　studies were aimed to explore the integration properties of GABA$_B$ receptor-mediated responses and
375　suggested a highly supralinear interaction through the amplification effect of G-protein cooperativity
376　(Destexhe, 1995). Our experimental approach indicates linear interactions between GABA$_B$ receptor
377　mediated responses in case the number of converging presynaptic cells corresponds to the number of
378　NGFCs cooperating during *in vivo* network operations. This suggests that converging afferents that act
379　on inhibitory metabotropic receptors in the same postsynaptic voxel show linear or slightly sublinear
380　summation, conserving the impact of individual inputs. However, we cannot exclude the possibility
381　that widespread synchronization across various interneuron populations might shift the summation
382　arithmetic in a nonlinear fashion.

383　Intrinsic properties of postsynaptic pyramidal cells might also contribute to the regulation of
384　summation. HCN1 channels are known to be enriched in the distal dendrites of pyramidal cells and
385　mediate K$^+$ cationic current activated by membrane hyperpolarization (Kalmbach et al., 2018; Lörincz
386　et al., 2002; Robinson & Siegelbaum, 2003) Our experiments presented above show that summation
387　properties in response to synchronized inputs from NGFCs are not significantly affected by HCN1
388　channels, presumably due to the relatively moderate local hyperpolarization arriving from NGFCs;
389　again, further studies are needed to test the influence of additional interneuron classes coactivated
390　together with NGFCs. We predict that further GABAergic activity is unlikely to change summation
391　arithmetics based on our negative results when blocking the high-affinity plasma membrane GABA
392　transporters concentrated in the perisynaptic and extrasynaptic areas (Melone, Ciappelloni, & Conti,
393　2015) effective in modulating GABA-mediated inhibition trough extrasynaptic GABA spillover (Barbour
394　& Häusser, 1997; Hamann, Rossi, & Attwell, 2002; Scanziani, 2000; Szabadics et al., 2007). Despite
395　having similar summation arithmetics of two consecutive APs to the triple-recording configuration, it
396　remains undefined as to what extent multiple presynaptic APs resemble synchronous activation of
397　individual release sites. Presynaptic GABA$_B$ receptor-mediated decrease in Ca^{2+} is unlikely (Karayannis
398　et al., 2010), however, depletion of the readily releasable pool of vesicles leading to synaptic
399　depression cannot be ruled out. As suggested by pioneering simulations on the summation of GABA$_B$
400　receptor-mediated signaling (Destexhe, 1995), a crucial intrinsic factor in the postsynaptic cells is the
401　molecular cascade linking GABA$_B$ receptors to the GIRK channels through G-proteins. Our experimental
402　evidence for close to linear or slightly sublinear summation of GABA$_B$ receptor-mediated responses
403　suggests that even if amplification through G-proteins plays a role, it is unable to overturn local
404　membrane or K$^+$ concentration dependent factors promoting sublinearity (Dascal, 1997; Inanobe &
405　Kurachi, 2014; Stanfield et al., 2002; Wickman & Clapham, 1995). Amplification of GIRK current by G-
406　proteins could be hampered by the need of cooperative action of up to four G-protein βγ subunits to
407　be effective in opening GIRK channels. In addition, hyperpolarization and the accompanying relatively
408　low [Na$^+$]$_i$ might also limit GIRK channel activation knowing that high [Na$^+$]$_i$ promotes GIRK channel
409　opening in depolarized cells (Wang et al., 2016). The latter scenario might promote a brain state-
410　dependent summation of metabotropic inhibitory signals in active neuronal networks, that remains to
411　be tested in future experiments. On the other hand, our ultrastructural model corroborates pioneering
412　suggestions (Á. Kulik et al., 2006; Qian & Sejnowski, 1990) that the effect of GABA$_B$ receptors is more
413　prominent on dendritic spines compared to dendritic shafts, having approximately twice the number
414　of activated GIRK channels per GABA$_B$ receptor on spines versus shafts. Admittedly, our simulations

415 could not cover the extensive intracellular signaling pathways known to be influenced by GABA$_B$
416 receptors (Gassmann & Bettler, 2012; Padgett & Slesinger, 2010; Terunuma, 2018) and future
417 availability of comprehensive transporter and extracellular space distributions of layer 1 would enrich
418 the model (Hrabetova, Cognet, Rusakov, & Nägerl, 2018; Korogod, Petersen, & Knott, 2015; Pallotto,
419 Watkins, Fubara, Singer, & Briggman, 2015). Nevertheless, our experiments and simulations suggest
420 that nonsynaptic GABAergic volume transmission providing relatively homogeneous and sufficient
421 concentrations of GABA combined with increased clustering of GABA$_B$ receptors and on spines
422 compared to shafts governs compartment dependent efficacy.

423 Taken together, our experimental results and modeling analysis suggest that a randomly chosen
424 location in the neuropil of layer 1 is targeted by a moderate number (usually one or two) presynaptic
425 NGFCs. In turn, there is no apparent gap in the neurogliaform coverage of layer 1, i.e. most elements
426 of the neuropil including classic postsynaptic compartments, presynaptic terminals or non-neuronal
427 cells are located sufficiently close to terminals of at least one NGFC and receive GABA nonsynaptically.
428 Interestingly, when two NGFCs which share target territory are coactivated or a single NGFC has a
429 limited number of consecutive spikes, linear arithmetics accompany GABA$_B$ receptor summation. This
430 supports the hypothesis that the density and distribution of neocortical NGFCs and their axonal
431 terminals combined with the effective range of GABAergic volume transmission appear optimized for
432 a spatially ubiquitous and predominantly linear metabotropic GABA$_B$ receptor summation.

433

Author Contributions

443 Conceptualization, G.T.; Methodology, A.O.,G.K.,G.M. and G.T.; Investigation, A.O.,G.K.,G.O. and J.B.;
444 Software, A.O.; Formal Analysis, A.O., G.K., G.O. and G.T.; Writing – Original Draft, A.O., G.K. and G.T.;
445 Writing – Review ̇& Editing, G.T.; Visualization, A.O.,G.K. and G.T.; Funding Acquisition, G.T.;
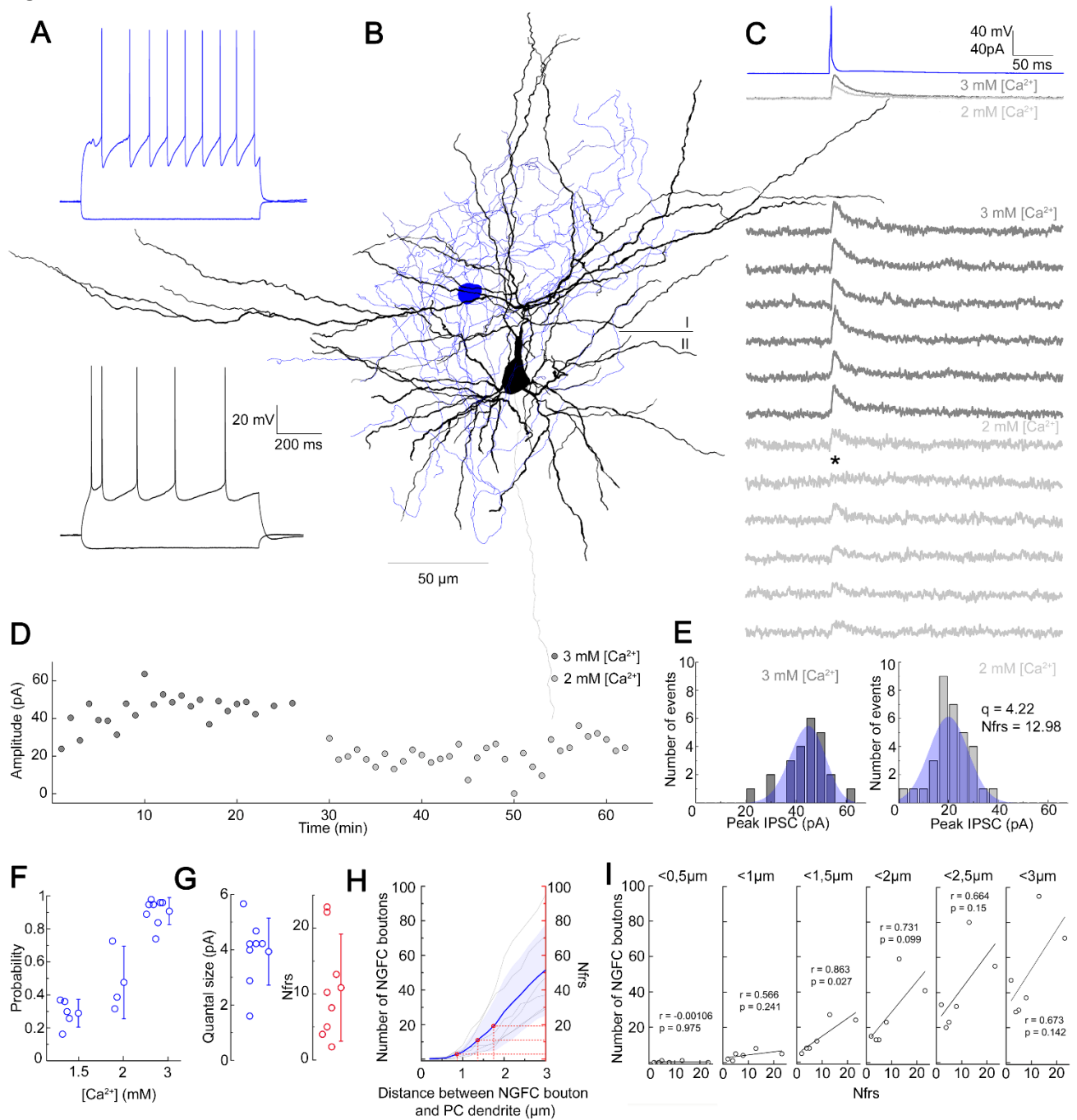446 Supervision, G.T.

Declaration of Interests

448 The authors declare no competing interest.

449

450

Figures

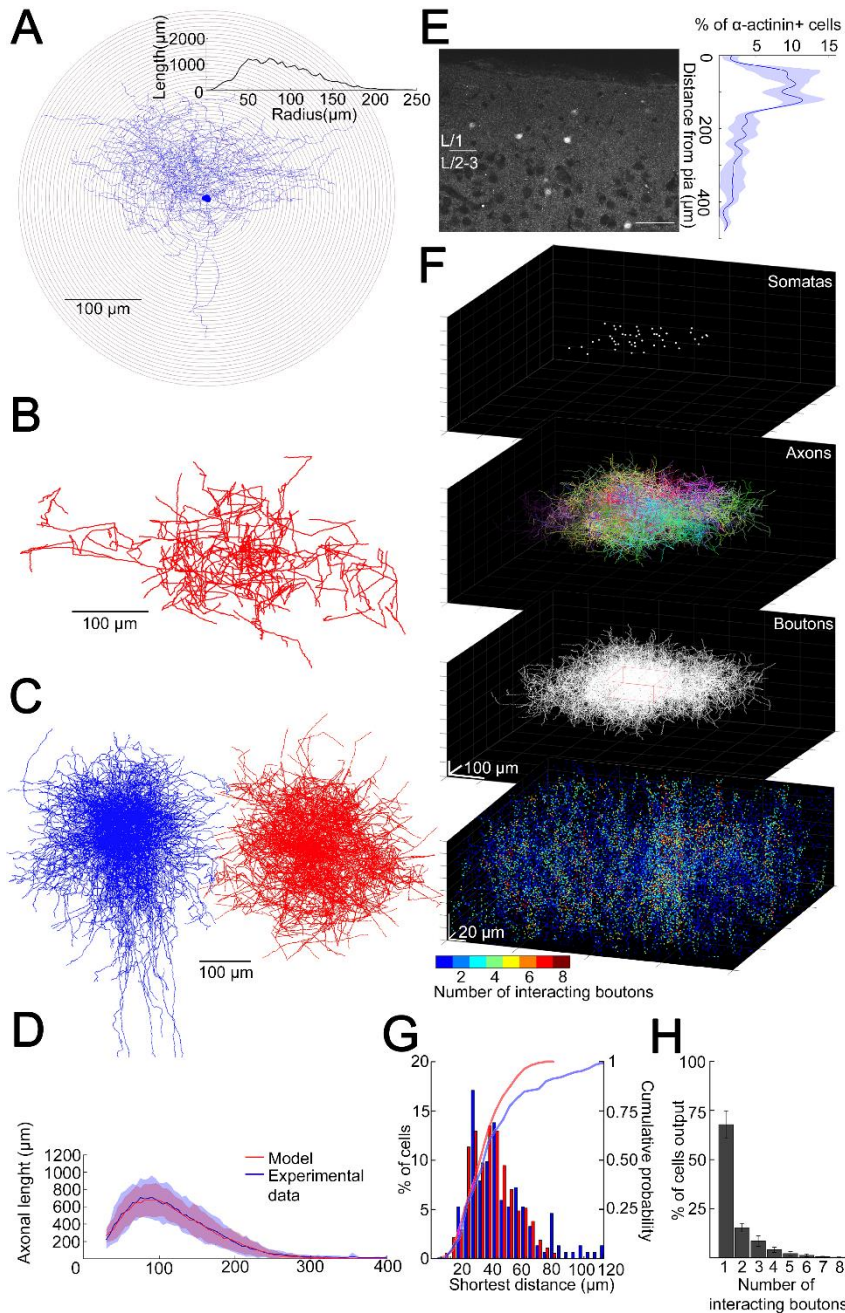**Figure 1. Quantal and structural characteristics of GABAergic connections established by individual neurogliaform cells**

(A) Firing patterns of the presynaptic NGFC (blue) and postsynaptic PC (black).

(B) Three-dimensional anatomical reconstruction of a recorded NGFC (soma and axon blue) and PC (soma and dendrites black, axon gray).

(C) Presynaptic action potentials of the NGFC (top, blue) elicited of unitary IPSCs in the postsynaptic PC at -50 mV holding potential in different Ca^{2+} concentrations (middle, dark gray: 3 mM Ca^{2+}, light gray 2 mM Ca^{2+}). Bottom, representative consecutive traces of elicited unitary IPSCs. Asterisk marks synaptic transmission failure.

(D) Single IPSC peak amplitudes recorded in high (3 mM Ca^{2+}, dark gray) and low release probability conditions (2 mM Ca^{2+}, light gray), respectively.

464   (E) Distribution of IPSC peak amplitudes in 3 mM [Ca^{2+}] (left) and 2 mM [Ca^{2+}] (right), with
465   projected binomial fits (blue).
466   (F) Estimated release probability values in different experimental conditions (n= 8).
467   (G) Estimated quantal size (3.93 ± 1.22 pA) and number of functional release sites (Nfrs; 10.96 ±
468   8.1) derived from Bayesian quantal analysis in each experiment (n= 8).
469   (H) Number of NGFC boutons in the proximity of postsynaptic PC dendrites from anatomical
470   reconstructions of connected NGFC to PC pairs (n= 8; gray, individual pairs; blue, average and
471   SD). For comparison, red lines indicate mean ± SD of Nfrs shown on panel F corresponding to
472   distances between presynaptic NGFC boutons and pyramidal cell dendrites.
473   (I) Number of NGFC boutons counted at increasing distances from PC dendrites in NGFC to PC
474   pairs. Correlation to Nfrs in the same pairs is best when counting boutons closer than 1.5 μm
475   from PC dendrites.

476
477 **Figure 2. Structural characteristics of collective GABAergic output formed by the population of layer**
478 **1 neurogliaform cells**

479   (A) Sholl analysis on the axonal arborization of an individual NGFC. Inset, axonal lengths measured
480   in concentric shells of increasing radius (step, 10 µm).
481   (B) Three-dimensional arborization of a model generated axon.
482   (C) Superimposition of three-dimensionally reconstructed axonal arborizations of NGFCs (n= 16,
483   blue) and the computer generated model NGFCs (n= 16, red) aligned at the center of somata.
484   (D) Comparison of manually reconstructed axonal arborizations of NGFCs (n= 16; blue, mean; light
485   blue, SD) and model generated axons (n= 52; red, mean; light red, SD)
486   (E) Left, α-actinin2 immunohistochemistry in supragranular layers of the neocortex. Right,
487   distribution of α-actinin2 immunopositive somata.
488   (F) Top, three-dimensional model of NGFCs somata, axonal arborizations and bouton distributions
489   in a 354 x 354 x 140 µm volume. Bottom, heat map showing the number of axonal boutons
490   interacting at distances of < 1.5 µm.
491   (G) Distribution of the shortest distance between somata in the model (red) and in α-actinin2
492   immunohistochemistry experiments (blue).
493   (H) Percentage distribution of the number of interacting boutons within 1.5 µm distance from
494   each NGFC.
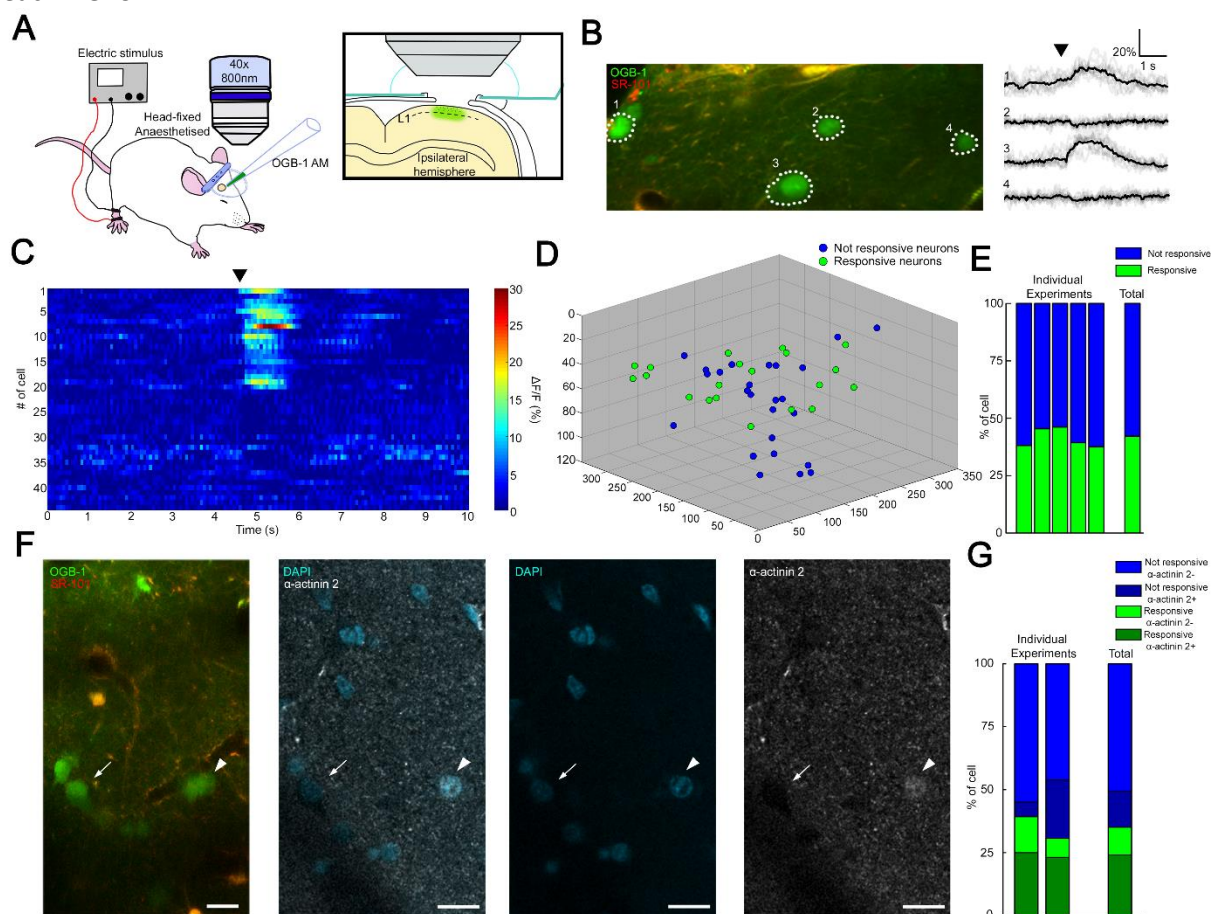
495
496   **Figure 3. Coactivation of neurogliaform cell population in L1 somatosensory cortex *in vivo***

497   (A) Experimental setup. Head-fixed anaesthetized rats were placed under a two-photon
498   microscope having a cranial window above the hindlimb somatosensory cortex. OGB-1 AM and
499   SR 101 were injected into L1. Ipsilateral hindlimb stimulation was performed with an electric
500   stimulator.
501   (B) Two-photon image of neurons that were labeled with OGB-1 in L1. SR 101 labeled astrocytes.
502   Right, ΔF/F changes of Ca^{2+} signals (grey: individual traces; black: mean of 10 consecutive
503   traces) during series of ipsilateral stimulation (black arrowhead). Traces correspond to the
504   marked cells.

505   (C) Time-series heat map of 44 L1 interneurons evoked $\Delta F/F$ changes in Ca^{2+} signals during
506   ipsilateral hindlimb stimulation (black arrowhead).
507   (D) Scatter plot showing the spatial location of L1 interneuron somata. Colors are corresponding
508   to the responsiveness (Not responsive, blue dots; responsive, green dots).
509   (E) Stack columns show the fraction of responsive versus not responsive cells in different
510   experiments (n= 5 animals). Far-right columns show the mean value.
511   (F) *In vivo* two-photon image showing imaged neurons. To the right, confocal images from the
512   same area shows immunohistochemical detection of α-actinin2+ neurons (arrowhead). α-
513   actinin2- cells were visualized by exclusive DAPI staining (arrow). Scale bar, 20 μm.
514   (G) Stack columns show the proportion of α-actinin2 immunoreactivity among responsive versus
515   not responsive cells (n= 2 animals). Far-right columns show the mean value.
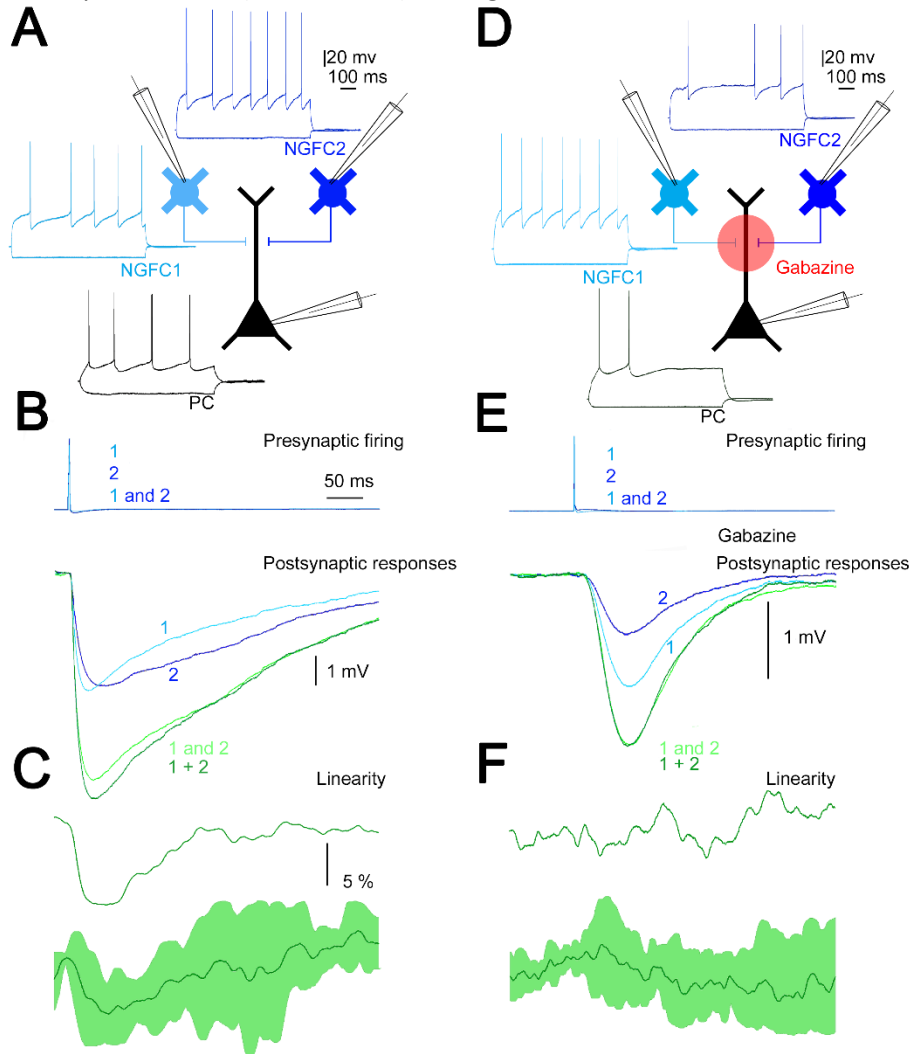
516
517   **Figure 4. Summation of convergent, unitary IPSPs elicited by neurogliaform cells**

518   (A) Schematic experimental setup of triplet recordings. Firing pattern of two presynaptic NGFCs
519   (light blue and blue) and a postsynaptic pyramidal cell (black).
520   (B) Action potential triggered under control conditions in the NGFCs individually (1, 2) or
521   synchronously (1 and 2) elicited unitary (1, 2) and convergent (1 and 2) IPSPs in the
522   postsynaptic PC. Below, the time course of the difference between the measured (1 and 2) and
523   calculated (1 + 2) sums of convergent IPSPs.
524   (C) The linearity of response summation on populations of convergent NGFC triggered IPSPs
525   recorded in control conditions (n= 4) (dark green, population average; light green, SD).
526   (D) Same as experimental setup as (A) but in the presence of GABA$_A$ receptor antagonist, gabazine.

527   (E)   Identical stimulation protocol as (B), note the disappearance of the difference between the
528   measured (1 and 2) and calculated (1 + 2) sums of convergent IPSPs.
529   (F) Same as (C), but under blocking $GABA_A$ receptors with gabazine (n= 8) (dark green, population
530   average; light green, SD).
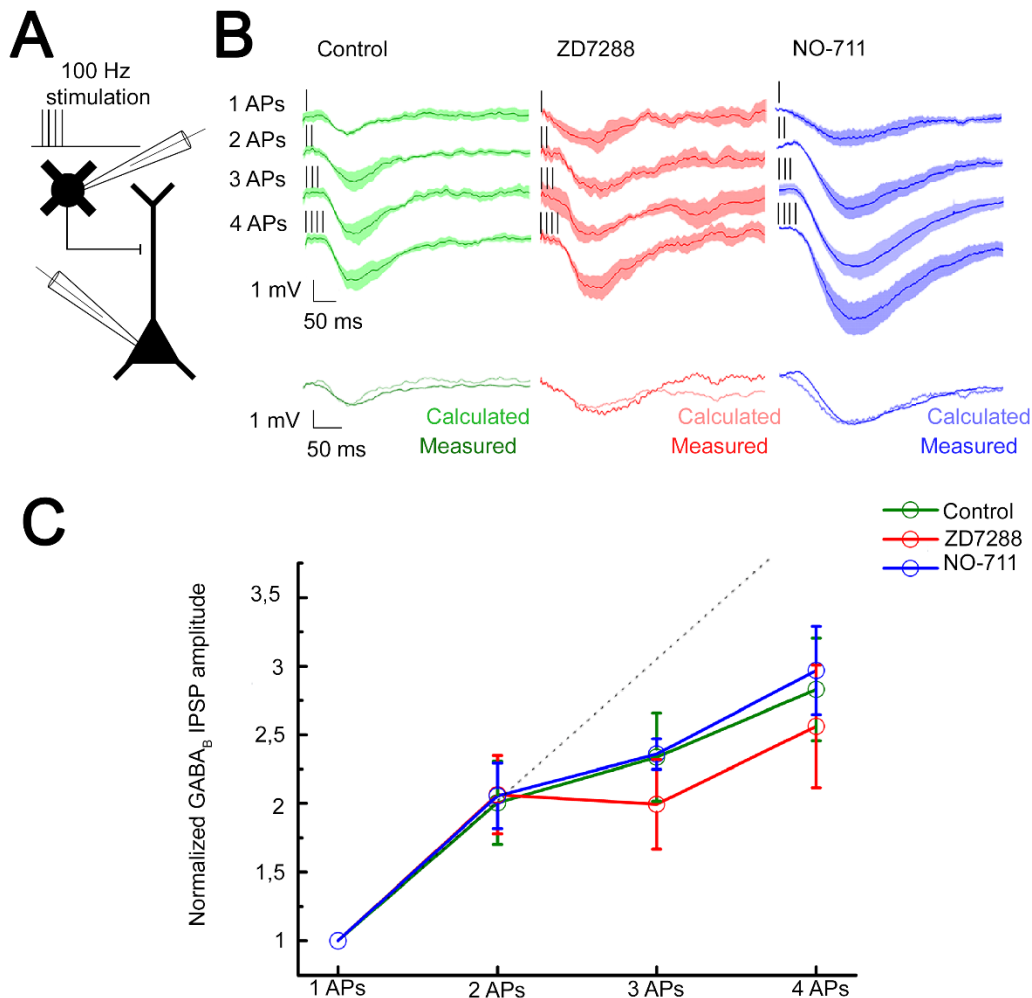
531
Figure 5. Integration of $GABA_B$ receptor-mediated responses are not affected by HCN channel and GABA reuptake

534   (A) Schematic experimental setup of paired recordings. Bursts of up to four action potentials (APs)
535   were elicited in NGFCs at 100 Hz in the presence of gabazine.
536   (B) NGFC to PC paired recordings showed similar linear $GABA_B$ receptor-mediated summation
537   under control conditions. Top, individual traces showing IPSP kinetics upon AP burst protocol
538   (vertical lines indicating the triggered APs) during control (green traces, n= 6), in presence of
539   hyperpolarization-activated cation (HCN) channel blocker ZD7288 (red traces, n= 5) or GABA
540   reuptake blocker NO-711 (blue traces, n= 6). Bottom, traces show measured IPSP from two
541   consecutive presynaptic stimulation (measured) and the arithmetic sum of two unitary IPSP
542   (calculated).
543   (C) Summary of normalized IPSP peak amplitudes. Compare to control conditions (2APs: 2.00 ±
544   1.08; 3APs: 2.34 ± 1.16; 4APs: 3.17 ± 1.26) summation properties of $GABA_B$ mediated unitary
545   IPSPs are not effected by application of ZD7288 (2APs: 2.06 ± 1.06, p= 0.983; 3APs: 1.99 ± 1.17,
546   p= 0.362; 4APs: 2.56 ± 1.6, p= 0.336; two-sided MW U test) neither NO-711 (2APs: 2.06 ± 1.17,
547   p= 0.853; 3APs: 2.36 ± 0.31, p= 0.645; 4APs: 2.9 7± 1.54, p= 0.515; two-sided MW U test).
548   Dashed line indicates the linearity.

549
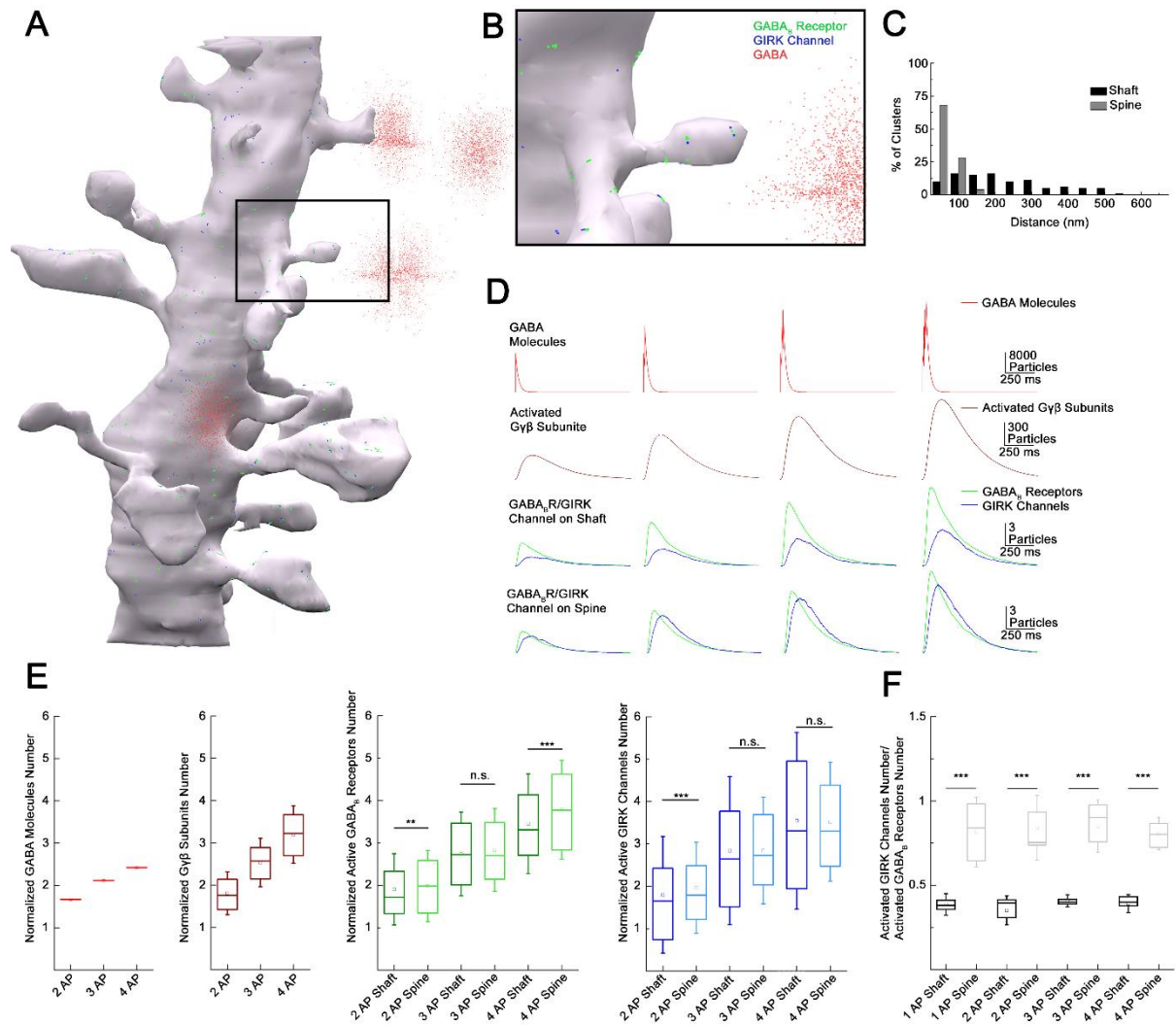
Figure 6. Subcellular localization of GABA$_B$ receptor-GIRK channel complex determines summation properties

(A) Visualization of the complete MCell based model in the course of GABA release.

(B) Magnified view of the model.

(C) Distribution of GABA$_B$ receptors and GIRK channel clusters on the dendritic membrane in the model (grey bars: dendritic spine; black bars: dendritic shaft).

(D) Overview of the molecular interactions during increasing GABA release. Top to bottom: NGFC output simulated by releasing GABA (red) in the extracellular space proportional to 1-4 action potential stimulation. Below, the total number of produced Gβγ subunits (brown) by activated GABA$_B$ receptors (green) located on the dendritic shaft and spine. After lateral diffusion in the plasma membrane, Gβγ subunits bind to GIRK channels (blue).

(E) Boxplot of GABA, Gβγ subunits, GABA$_B$ receptors and GIRK channels quantity normalized to 1AP (GABA: 2APs: 1.67 ± 0.004, 3APs: 2.12 ± 0.005, 4APs: 2.42 ± 0.006, Gβγ subunits: 2APs: 1.85 ± 0.51, 3APs: 2.53 ± 0.57, 4APs: 3.2 ± 0.68; GABA$_B$ receptor shaft: 2APs: 1.91 ± 0.84, 3APs: 2.74 ± 0.99, 4APs: 3.45 ± 1.18; GABA$_B$ receptor spine: 2APs: 1.98 ± 0.84, 3APs: 2.84 ± 0.98, 4APs: 3.78 ± 1.17; GIRK channel shaft: 2APs: 1.8 ± 1.37, 3APs: 2.84 ± 1.75, 4AP: 3.55 ± 2.09; GIRK channel spine: 2APs: 1.96±1.07, 3APs: 2.84 ± 1.26, 4APs: 3.52 ± 1.4). Square indicate the mean, line shows the median inside the boxplot.

(F) Quantification of the signaling effectiveness on the shaft and spine region of the model dendrite during increasing GABA release (1AP: shaft: 0.39 ± 0.06, spine: 0.82 ± 0.21, p < 0.005, n= 1164, two-sided MW U test; 2AP: shaft: 0.35 ± 0.086, spine: 0.84 ± 0.19, p < 0.005, n= 534,

571   two-sided MW U test; 3AP: shaft: ± 0.41 ± 0.036, spine: 0.85 ± 0.15, $p < 0.005$, n= 1871, two-

572   sided MW U test; 4AP: shaft: 0.39 ± 0.05, spine: 0.81 ± 0.01, $p < 0.005$, n= 709, two-sided MW

573   U test). Square indicate the mean, line shows the median inside the boxplot.

574

575

576

Methods

Slice preparation

Experiments were conducted to the guidelines of University of Szeged Animal Care and Use Committee. We used young adult (19 to 46-days-old, (P) 23.9 ± 4.9) male Wistar rats for the electrophysiological experiments. Animals were anaesthetized by inhalation of halothane, and following decapitation, 320 μm thick coronal slices were prepared from the somatosensory cortex with a vibration blade microtome (Microm HM 650 V; Microm International GmbH, Walldorf, Germany). Slices were cut in ice-cold (4^oC) cutting solution (in mM) 75 sucrose, 84 NaCl, 2.5 KCl, 1 NaH_2PO_4, 25 $NaHCO_3$, 0.5 $CaCl_2$, 4 $MgSO_4$, 25 d (+)-glucose, saturated with 95% O_2 and 5% CO_2. The slices were incubated in 36^oC for 30 minutes, subsequently the solution was changed to (in mM) 130 NaCl, 3.5 KCl, 1 NaH_2PO_4, 24 $NaHCO_3$, 1 $CaCl_2$, 3 $MgSO_4$, 10 d (+)-glucose, saturated with 95% O_2 and 5% CO_2, and the slices were kept in it until experimental use. The solution used for recordings had the same composition except that the concentrations of $CaCl_2$ and $MgSO_4$ were 3 mM and 1.5 mM unless it is indicated otherwise. The micropipettes (3-5 MΩ) were filled (in mM) 126 K-gluconate, 4 KCl, 4 ATP-Mg, 0.3 GTP-Na_2, 10 HEPES, 10 phosphocreatine, and 8 biocytin (pH 7.25; 300 mOsm).

In vitro Electrophysiology and Pharmacology

Somatic whole-cell recordings were obtained at ~37^oC from simultaneously recorded triplets and doublets of NGF and PC cell visualized by infrared differential interference contrast video microscopy at depths 60-160 μm from the surface of the slice (Zeiss Axio Examiner LSM7; Carl Zeiss AG, Oberkochen, Germany), 40x water-immersion objective (1.0 NA; Carl Zeiss AG, Oberkochen, Germany) equipped with Luigs and Neumann Junior micromanipulators (Luigs and Neumann, Ratingen, Germany) and HEKA EPC 10 patch clamp amplifier (HEKA Elektronik GmbH, Lambrecht, Germany). Signals were filtered 5 kHz, digitalized at 15 kHz, and analyzed with Patchmaster software. Presynaptic cells were stimulated with a brief suprathreshold current pulse (800 pA, 2-3 ms), derived in >60 s interval. In experiments, where two presynaptic NGFC were stimulated simultaneously the interval was increased >300 s. The stimulation sequence, in which one or the other or both presynaptic NGFCs were stimulated was constantly altered, therefore the potential rundown effect or long term potentiation would affect all three stimulation condition equally. In the case of 100 Hz presynaptic burst stimulation the interval was increased >300 s. During stimulation protocol, the order of triggering a set of 1 to 4 APs on the NGFc were randomized. The postsynaptic responses were normalized to the single AP in each individual set. During postsynaptic current-clamp recording -50 mV holding current was set. The experiments were stopped if the series resistance (Rs) exceeded 35 MOhm or changed more than 20%. During postsynaptic voltage-clamp recordings, Rs and whole-cell capacitance were monitored continuously. The experiment was discarded if the compensated Rs change reached 20% during recording.

Pharmacological experiments were carried out on NGFC-PC pairs using ACSF with the following drugs: 10 μM SR 95531 hydrobromide (Tocris), 10 μM D- (-)-2-Amino-5-phosphonopentanoic acid (D-AP5) (Tocris), 10 μM 2,3-Dioxo-6-nitro-1,2,3,4-tetrahydrobenzo[*f*]quinoxaline-7-sulfonamide (NBQX) (Tocris), 10 μM 4- (N-Ethyl-N-phenylamino)-1,2 dimethyl-6- (methylamino) pyrimidinium chloride (ZD7288) (Sigma-Aldrich), 10 μM 1-[2-[[(Diphenylmethylene)imino]oxy]ethyl]-1,2,5,6-tetrahydro-3-pyridinecarboxylic acid hydrochloride hydrochloride (NO711) (Sigma-Aldrich).

We performed Bayesian quantal analysis (BQA) by altering the extracellular Ca^{2+} and Mg^{2+} in two different conditions (Bhumbra & Beato, 2013a). One of the conditions were provide consistently a high release probability, in which the ACSF contained (in mM): 3 Ca^{2+} / 1.5 Mg^{2+}. For the reduced release probability we tested two different composition (in mM): either 2 Ca^{2+} / 2 Mg^{2+} or 1.5 Ca^{2+}/ 3 Mg^{2+}. During BQA experiments the ACSF solution contained the following substances: 10 μM D- (-)-2-Amino-5-phosphonopentanoic acid (D-AP5) (Tocris), 10 μM 2,3-Dioxo-6-nitro-1,2,3,4-tetrahydrobenzo[*f*]quinoxaline-7-sulfonamide (NBQX) (Tocris). Each epoch of the BQA experiment

626   contains a stable segment of 28 up to 42 unitary IPSCs (mean 32.75 ± 4.15). BQA experiments required
627   at least 60 min of recording time (up to 90 minutes). We tested all epochs for possible long-term
628   plasticity effect by measuring the linear correlation between IPSCs amplitude and elapsed time during
629   the experiment, and we found no or negligible correlation (Pearson's r values from all of the
630   experiments (n= 8) were between -0.39 and 0.46, mean -0.01 ± 0.29).

631

632   **Immunohistochemistry and anatomical analysis**
633   After electrophysiological recordings slices were fixed in a fixative containing 4% paraformaldehyde,
634   15% picric acid and 1.25% glutaraldehyde in 0.1 M phosphate buffer (PB; pH= 7.4) at 4°C for at least
635   12 hr. After several washes in 0.1 M PB, slices were cryoprotected in 10% then 20% sucrose solution in
636   0.1 M PB. Slices were frozen in liquid nitrogen then thawed in PB, embedded in 10% gelatin and further
637   sectioned into slices of 60 μm in thickness. Sections were incubated in a solution of conjugated avidin-
638   biotin horseradish peroxidase (ABC; 1:100; Vector Labs) in Tris-buffered saline (TBS, pH= 7.4) at 4°C
639   overnight. The enzyme reaction was revealed by 3'3-diaminobenzidine tetrahydrochloride (0.05%) as
640   chromogen and 0.01% H_2O_2 as an oxidant. Sections were post-fixed with 1% OsO_4 in 0.1 M PB. After
641   several washes in distilled water, sections were stained in 1% uranyl acetate, dehydrated in ascending
642   series of ethanol. Sections were infiltrated with epoxy resin (Durcupan (Sigma-Aldich)) overnight and
643   embedded on glass slices. Three dimensional light microscopic reconstructions were carried out using
644   Neurolucida system with a 100x objective.

645

646   **Surgery for imaging experiments**
647   Experiments were conducted to the guidelines of University of Szeged Animal Care and Use
648   Committee. Young adult (22 to 28 days old, (P) 24.75 ± 2.75) male Wistar rats were initially
649   anaesthetized with halothane before urethane anaesthesia (1.4 g/kg of body weight) was
650   administrated intraperitoneally. Body temperature was maintained at 37°C with a heating pad
651   (Supertech Instruments, Pécs, Hungary). Before surgery dexamethasone sodium phosphate (2 mg/kg
652   of body weight) was administrated subcutaneous, and carprofen (5 mg/kg of body weight) was
653   administrated intraperitoneally. Anaesthetized animals head were stabilized in a stereotaxic frame and
654   headbars were attached to the skull with dental cement (Sun Medical, Mariyama, Japan). Circular
655   craniotomy (3 mm diameter) was made above the primary somatosensory cortex, centered at 1.5 mm
656   posterior and 2.2 mm lateral from the bregma with a high-speed dental drill (Jinme Dental, Foshan,
657   China). Dura mater was carefully removed surgically. Finally, the craniotomy was filled with 1.5 %
658   agarose and covered with a coverslip to limit motion artifacts. The craniotomy was then submerged
659   with HEPES buffered ACSF recording solution containing (in mM) 125 NaCl, 3.5 KCl, 10 HEPES, 1 $MgSO_4$,
660   1 $CaCl_2$, 0.5 d (+)-glucose, pH= 7.4.

661

662   **Two photon calcium imaging in L1**
663   Before covering the craniotomy with the coverslip calcium indicator Oregon Green 488 BAPTA-1 AM
664   (10mM) (OGB-1 AM, Thermo Fisher Scientific), and astrocytic marker sulforhodamine 101 (1 μM)
665   (SR101, Thermo Fisher Scientific) were pressure-injected with a glass pipette (1-2 MΩ) in L1 cortical
666   region under the visual guide of Zeiss Axio Examiner LSM7 (Carl Zeiss AG, Oberkochen, Germany) two-
667   photon microscope using 40x water immersion objective (W-Plan, Carl Zeiss, Germany). Subsequently,
668   the craniotomy was filled with agarose and covered with a coverslip. Imaging experiments were
669   performed 1 hour after preparation. The activity of L1 interneurons was monitored during ipsilateral
670   hindlimb electrical stimulation (Digimeter, Hertfordshire, United Kingdom, 200 mA, 10 ms). OGB-1 AM
671   was excited at 800 nm wavelength with a femtosecond pulsing Ti:sapphire laser (Mai Tai DeepSee
672   (Spectra-physics, Santa Clara, USA)). In the somatosensory hindlimb region, Z-stack image series
673   (volume size 304 μm x 304 μm x 104 μm) were acquired. Calcium signals from interneurons were

674   obtained within this volume in full-frame mode (256 x 100 pixel), acquired at a frequency of ~20 Hz.
675   The Ca^{2+} dependent fluorescence change ΔF/F was calculated as $R(t)=(F(t)-F_0(t))/F_0(t)$ based on Jia et al
676   2010 (Jia, Rochefort, Chen, & Konnerth, 2011). The R(t) denotes the relative change of fluorescence
677   signal, F(t) denotes the mean fluorescence of a region of interest at a certain time point, $F_0(t)$ denotes
678   the time-dependent baseline. Image stabilization was performed by ImageJ (Fiji) software using the
679   Image stabilizer plugin (Kang Li, 2008; Schneider, Rasband, & Eliceiri, 2012). At the end of the
680   experiments, few L1 neurons were filled with biocytin containing intracellular solution to make the
681   immunohistochemical remapping easier.

682

Tissue preparation for immunohistochemistry
684   After imaging experiments rats were deeply anaesthetized with ketamine and xylazine. Subsequently,
685   perfusion was performed through the aorta, first with 0.9% saline for 1 min, then with an ice-cold
686   fixative containing 4% paraformaldehyde in 0.1 M phosphate buffer (PB, pH= 7.4) for 15 min. The
687   whole brain was extracted and stored in 4% paraformaldehyde for 24 hours, afterward in 0.1 M
688   phosphate buffer (pH= 7.4) until slicing. Later 60 µm thick sections were cut from the same two-photon
689   Ca^{2+} imaged brain area parallel to the pia mater and washed overnight in 0.1 M PB.

690

Fluorescence immunohistochemistry and remapping
692   After several washes in 0.1 M PB, slices were cryoprotected with 10% then 20% sucrose solution in
693   0.1M PB than frozen in liquid nitrogen. The sections were incubated for two hours in Alexa-488
694   conjugated streptavidin (1:400, Molecular Probes) solved in Tris-buffered saline (TBS, 0.1 M; pH= 7.4)
695   at room temperature to visualized the biocytin labeled cells. After several washes in TBS, sections were
696   blocked in normal horse serum (NHS, 10%) made up in TBS, followed by incubation in mouse anti-Alfa-
697   Actinin (1:20000, Sigma-Aldrich) diluted in TBS containing 2% NHS and 0.1% Triton X-100 at room
698   temperature for 6 hours. Following several washes in TBS, Cy3 conjugated donkey anti-mouse (1:500,
699   Jackson ImmunoResearch) secondary antibody was used to visualize the immunoreactions. After
700   several washes in TBS then in 0.1 M PB, slices were counterstained with DAPI (4' ,6-diamidino-2-
701   phenylindole, ThermoFisher Scientific). Sections were then mounted on slides in Vectashield (Vector
702   Laboratories). Images were taken with LSM 880 confocal laser scanning microscope (Carl Zeiss AG,
703   Oberkochen, Germany) using 40X oil-immersion objective (1.4 NA). Confocal image z-stack was tilted
704   and panned manually to match with the *in vivo* two photon z-stack, allowing to profile imaged
705   interneurons. During this process biocytin labeled neurons were used as a reference point.

706

Data analysis
708   Electrophysiological data were analyzed with Fitmaster (HEKA Elektronik GmbH, Lambrecht,
709   Germany), Origin 7.5 (OriginLab Corporation, Northampton, Massachusetts, USA), IgorPro
710   (Wavemetrics, Portland, Oregon, USA). BQA experiments were analyzed using a Python written
711   program (Bhumbra & Beato, 2013a), incorporating NumPy and SciPy packages. Two-photon calcium
712   imaging data were acquired with ZEN 2 (Carl Zeiss AG, Oberkochen, Germany) and analyzed with
713   MATLAB (The MathWorks, Natick, Massachusetts, USA), using Statistical Toolbox, Image Processing
714   Toolbox, and custom written scripts.

715

MCell model construction

717   The model framework was constructed in Blender v2.7. The simulation environment contained a 3D
718   reconstruction of a dendritic structure based on a series section of electron microscopic data (available
719   from VolRoverN program (Edwards et al., 2014)), and realistically positioned release sites of NGFCs. In
720   the simulation environment the extracellular space was also modeled by creating an array of cubic
721   cells containing cavities based on previous work from Tao et al (Tao et al., 2005). The cubic cells have

722 800 x 800 nm length, containing cavity that is 400 x 400 nm wide and 340 nm deep. The cubic cells and
723 the dendritic segment were spaced 32 nm apart. The established array of cubic compartments creates
724 an extracellular space that provides a volume fraction and tortuosity identical to the cortical brain
725 tissue (volume fraction = 0.2 and tortuosity= 1.6). The overall dimensions of the modeled space
726 surrounding the ultrastructurally reconstructed dendrite were 13.28 x 13.28 x 6.592 µm and the total
727 volume was 1162.55 µm^3.

728 Simulation of $GABA_B$ receptor- GIRK channel interaction was carried out with MCell v3.4
729 (www.mcell.org)(Kerr et al., 2008). Custom Matlab scripts created the MDL (Model Description
730 Language) file that required for MCell simulation. MCell simulated the release and diffusion of GABA,
731 $GABA_B$ receptors and GIRK channel interaction. First, to manage a biological like distribution for the
732 receptors and channels a reaction cascade was used (Supplemetary Fig. 3). This cascade was
733 constructed and tested in a simple simulation environment first, containing only a plane surface. At
734 the beginning of every iteration, primary seed particles were placed on the dendritic membrane.
735 Primary seed particles subdivide into secondary seed particles, that which then produce $GABA_B$
736 receptor or GIRK channel clusters. Those secondary seed particles that produce the GIRK channel
737 clusters - which contain 1 to 4 channels - were immobile in the membrane. Meanwhile, the secondary
738 seed particles that produce $GABA_B$ receptor clusters – which contain 1 to 8 receptors – can diffuse
739 laterally in the membrane. At the end the distance was defined between the center of receptor and
740 channel clusters by calculating the distance between each receptor and channel cluster in the two-
741 dimensional plane surface. delay and the forward rate of the reaction was set to allow secondary
742 seeds, that generate $GABA_B$ receptor clusters to diffuse to specified distance, resulting in the required
743 $GABA_B$ receptor-GIRK channel cluster distribution as seen from Kulik et al (A. Kulik, 2006). Optimization
744 algorithm based on simulated annealing technique (Henderson, Jacobson, & Johnson, 2006;
745 Kirkpatrick, Gelatt, & Vecchi, 1983) was written in Matlab for approximating the optimal values for the
746 delay and the forward rate of the reaction. Optimal values of delay and the forward rate of the reaction
747 was set to allow secondary seeds, that generate $GABA_B$ receptor clusters to diffuse to specified
748 distance, resulting in the required $GABA_B$ receptor-GIRK channel cluster distribution as seen in Kulik et
749 al. 2005.

750 Since we were interested in the interaction between the $GABA_B$ receptors and GIRK channels, our
751 model does not include $GABA_A$ receptors and GABA amino transporters. Previous work suggest that a
752 single AP in the NGFC generates GABA concentration of 1 to 60 µM lasting for 20-200 ms (Karayannis
753 et al., 2010), therefore in our model we used similar GABA concentration range of at 0.5 to 2 µm
754 distance from the release sites.

755 Up to 6 MCell simulations were run with 1 µs time steps in parallel on pc with Intel (R) Core i7-4790
756 3.6 GHz CPU, 32 GB RAM. Total of 4278 iterations were simulated.

757

758 **Statistics**
759 The number of experimental recordings used in each experiment is indicated in the text. Statistical
760 tests were performed using Origin 7.5 (OriginLab Corporation, Northampton, Massachusetts, USA) and
761 SPSS software (IBM, Armonk, NY, USA). Data are represented as mean ± standard deviation (SD). Data
762 were first subject to a Shapiro-Wilk test of normality, and based on the result to the indicated
763 parametric and non-parametric tests. Result were considered significantly different if p<0.05.
764

765

766

767

768   Table 1. Parameters used for simulation

Parameter	Value	References
Total dendritic surface	31,204 μm^2	
Dendritic spines surface	15,621 μm^2	
Dendritic shaft surface	15,583 μm^2	
GABA$_B$ receptor density	36 particles/μm^2	(Degro, Kulik, Booker, & Vida, 2015)Degro et al., 2015
GIRK channel density	12,2 particles/μm^2	(Degro et al., 2015)Degro et al., 2015
Number of GABA molecules released/release site	3750	
Free GABA diffusion coefficient	0.76 μm^2/ms	(Longsworth, 1952)Longsworth, 1952
GABA$_B$R Kon rate	$5*10^6$ $M^{-1}s^{-1}$	(Sodickson & Bean, 1996)Sodickson and Bean, 1996; (Beenhakker & Huguenard, 2010)Beenhakker and Huguenard, 2010
GABA$_B$R Koff rate	5 s^{-1}	(Sodickson & Bean, 1996)Sodickson and Bean, 1996; (Beenhakker & Huguenard, 2010)Beenhakker and Huguenard, 2010
Membrane associated molecules diffusion	$4*10^{-9}$ cm^2/s	(Perez et al., 2006)Perez, 2006
G-protein Kon rate	$6*10^7$ $M^{-1}s^{-1}$	(Brinkerhoff et al., 2008)Brinkerhoff, 2008
G-protein hydrolysis	2-3 s^{-1}	(Breitwieser & Szabo, 1988)Breitweiser and Szabo, 1988
G-protein concentration	1200 /μm^2	(Wang et al., 2016)Wang et al., 2016
1st G-protein- GIRK Kon rate	$2,6*10^5$ $M^{-1}s^{-1}$	(Wang et al., 2016)Wang et al., 2016
2st G-protein- GIRK Kon rate	$5*10^5$ $M^{-1}s^{-1}$	Supposition based on Wang et al 2016
3st G-protein- GIRK Kon rate	$1,6*10^6$ $M^{-1}s^{-1}$	Supposition based on Wang et al 2016
4st G-protein- GIRK Kon rate	10^7 $M^{-1}s^{-1}$	(Wang et al., 2016)Wang et al., 2016
G-protein – GIRK Koff rate	500 s^{-1}	
G-protein (gamma-beta) –G (alpha) Kon	$0.7*10^6$ $M^{-1}s^{-1}$	(Yakubovich et al., 2015)Yakubovich et al 2015
G-protein (gamma-beta) –G (alpha) Koff	0,0013 s^{-1}	(Yakubovich et al., 2015)Yakubovich et al 2015
GABA$_B$R activation time	50 ms	(Sodickson & Bean, 1996)Sodickson and Bean, 1996
Gaba$_B$R deactivation	150 ms	(Sodickson & Bean, 1996)Sodickson and Bean, 1996
Gaba$_B$R inactivation	1 s	(Sodickson & Bean, 1996)Sodickson and Bean, 1996
GIRK open time	0.9 ms	(Velimirovic, Gordon, Nancy F Lim, & Clapham, 1996)Velimirovic et al., 1996
Simulation time steps	10^{-5} s	
Simulation Iterations	10^5	

769

770   **References**

771   Ascoli, G. A., Alonso-Nanclares, L., Anderson, S. a, Barrionuevo, G., Benavides-Piccione, R., Burkhalter,
772   A., … Yuste, R. (2008). Petilla terminology: Nomenclature of features of GABAergic interneurons
773   of the cerebral cortex. *Nature Reviews Neuroscience*. https://doi.org/10.1038/nrn2402

774   Barbour, B., & Häusser, M. (1997). Intersynaptic diffusion of neurotransmitter. *Trends in
775   Neurosciences*, *20*(9), 377–384. https://doi.org/10.1016/s0166-2236(96)20050-5

776   Barker, B. Y. J. L., Ransom, B. R., & Neurobiology, D. (2009). AMINO ACID PHARMACOLOGY OF
777   MAMMALIAN CENTRAL From the Laboratory of Neurophysiology , NINCDS ,. *Journal of
778   Physiology*, (1978), 331–354.

779   Beenhakker, M. P., & Huguenard, J. R. (2010). Astrocytes as Gatekeepers of GABAB Receptor
780   Function. *Journal of Neuroscience*, *30*(45), 15262–15276.
781   https://doi.org/10.1523/jneurosci.3243-10.2010

782   Berger, T., Larkum, M. E., & Lüscher, H. R. (2001). High I(h) channel density in the distal apical
783   dendrite of layer V pyramidal cells increases bidirectional attenuation of EPSPs. *Journal of
784   Neurophysiology*, *85*(2), 855–868. https://doi.org/10.1152/jn.2001.85.2.855

785   Bettler, B., Kaupmann, K., Mosbacher, J., & Gassmann, M. (2004). Molecular Structure and
786   Physiological Functions of GABA B Receptors . *Physiological Reviews*, *84*(3), 835–867.
787   https://doi.org/10.1152/physrev.00036.2003

788   Bezaire, M. J., Raikov, I., Burk, K., Vyas, D., & Soltesz, I. (2016). Interneuronal mechanisms of
789   hippocampal theta oscillations in a full-scale model of the rodent CA1 circuit. *ELife*, *5*.
790   https://doi.org/10.7554/eLife.18566

791 Bhumbra, G. S., & Beato, M. (2013a). Reliable evaluation of the quantal determinants of synaptic
792   efficacy using Bayesian analysis. *Journal of Neurophysiology*, *109*(2), 603–620.
793   https://doi.org/10.1152/jn.00528.2012

794 Bhumbra, G. S., & Beato, M. (2013b). Reliable evaluation of the quantal determinants of synaptic
795   efficacy using Bayesian analysis. *Journal of Neurophysiology*, *109*(2), 603–620.
796   https://doi.org/10.1152/jn.00528.2012

797 Bloss, E. B., Cembrowski, M. S., Karsh, B., Colonell, J., Fetter, R. D., & Spruston, N. (2016). Structured
798   Dendritic Inhibition Supports Branch-Selective Integration in CA1 Pyramidal Cells. *Neuron*, *89*(5),
799   1016–1030. https://doi.org/10.1016/j.neuron.2016.01.029

800 Breitwieser, G. E., & Szabo, G. (1988). Mechanism of muscarinic receptor-induced K+ channel
801   activation as revealed by hydrolysis-resistant GTP analogues. *The Journal of General Physiology*,
802   *91*(4), 469–493. https://doi.org/10.1085/jgp.91.4.469

803 Brinkerhoff, C. J., Choi, J. S., & Linderman, J. J. (2008). Diffusion-limited reactions in G-protein
804   activation: Unexpected consequences of antagonist and agonist competition. *Journal of
805   Theoretical Biology*, *251*(4), 561–569. https://doi.org/10.1016/j.jtbi.2008.01.002

806 Capogna, M. (2011). Neurogliaform cells and other interneurons of stratum lacunosum-moleculare
807   gate entorhinal-hippocampal dialogue. *The Journal of Physiology*, *589*(8), 1875–1883.
808   https://doi.org/10.1113/jphysiol.2010.201004

809 Capogna, M., & Pearce, R. A. (2011). GABA A,slow: causes and consequences. *Trends in
810   Neurosciences*, *34*(2), 101–112. https://doi.org/10.1016/j.tins.2010.10.005

811 Craig, M. T., Mayne, E. W., Bettler, B., Paulsen, O., & McBain, C. J. (2013). Distinct roles of GABAB1a-
812   and GABAB1b-containing GABAB receptors in spontaneous and evoked termination of
813   persistent cortical activity. *The Journal of Physiology*, *591*(Pt 4), 835–843.
814   https://doi.org/10.1113/jphysiol.2012.248088

815 Dascal, N. (1997). Signalling Via the G Protein-Activated K+ Channels. *Cellular Signalling*, *9*(8), 551–
816   573. https://doi.org/10.1016/S0898-6568(97)00095-8

817 Degro, C. E., Kulik, A., Booker, S. A., & Vida, I. (2015). Compartmental distribution of GABAB receptor-
818   mediated currents along the somatodendritic axis of hippocampal principal cells. *Frontiers in
819   Synaptic Neuroscience*, *7*(MAR), 6. https://doi.org/10.3389/fnsyn.2015.00006

820 Destexhe, A. (1995). G protein activation kinetics and spillover of GABA may account for differences
821   between inhibitory responses in the hippocampus and thalamus. *Neurobiology*, *92*(October),
822   9515–9519.

823 Dutar, P., & Nicoll, R. A. (1988). A physiological role for GABAB receptors in the central nervous
824   system. *Nature*, *332*(6160), 156–158. https://doi.org/10.1038/332156a0

825 Edwards, J., Daniel, E., Kinney, J., Bartol, T., Sejnowski, T., Johnston, D., … Bajaj, C. (2014). VolRoverN:
826   Enhancing Surface and Volumetric Reconstruction for Realistic Dynamical Simulation of Cellular
827   and Subcellular Function. *Neuroinformatics*, *12*(2), 277–289. https://doi.org/10.1007/s12021-
828   013-9205-2

829 Farrant, M., & Nusser, Z. (2005). Variations on an inhibitory theme: phasic and tonic activation of
830   GABA(A) receptors. *Nature Reviews. Neuroscience*, *6*(3), 215–229.
831   https://doi.org/10.1038/nrn1625

832 Gassmann, M., & Bettler, B. (2012). Regulation of neuronal GABAB receptor functions by subunit
833   composition. *Nature Reviews Neuroscience*, *13*(6), 380–394. https://doi.org/10.1038/nrn3249

834   Gonzalez-Burgos, G., Rotaru, D. C., Zaitsev, A. V., Povysheva, N. V., & Lewis, D. A. (2009). GABA
835   Transporter GAT1 Prevents Spillover at Proximal and Distal GABA Synapses Onto Primate
836   Prefrontal Cortex Neurons. *Journal of Neurophysiology*, *101*(2), 533–547.
837   https://doi.org/10.1152/jn.91161.2008

838   Hamann, M., Rossi, D. J., & Attwell, D. (2002). Tonic and spillover inhibition of granule cells control
839   information flow through cerebellar cortex. *Neuron*, *33*(4), 625–633.
840   https://doi.org/10.1016/S0896-6273(02)00593-7

841   Hao, J., Wang, X. -d., Dan, Y., Poo, M. -m., & Zhang, X. -h. (2009). An arithmetic rule for spatial
842   summation of excitatory and inhibitory inputs in pyramidal neurons. *Proceedings of the*
843   *National Academy of Sciences*, *106*(51), 21906–21911.
844   https://doi.org/10.1073/pnas.0912022106

845   Henderson, D., Jacobson, S. H., & Johnson, A. W. (2006). The Theory and Practice of Simulated
846   Annealing. In *Handbook of Metaheuristics* (pp. 287–319). Boston: Kluwer Academic Publishers.
847   https://doi.org/10.1007/0-306-48056-5_10

848   Hrabetova, S., Cognet, L., Rusakov, D. A., & Nägerl, U. V. (2018). Unveiling the extracellular space of
849   the brain: From super-resolved microstructure to in vivo function. *Journal of Neuroscience*,
850   *38*(44), 9355–9363. https://doi.org/10.1523/JNEUROSCI.1664-18.2018

851   Huguenard, J. R., & Alger, B. E. (1986). Whole-cell voltage-clamp study of the fading of GABA-
852   activated currents in acutely dissociated hippocampal neurons. *Journal of Neurophysiology*,
853   *56*(1), 1–18. https://doi.org/10.1152/jn.1986.56.1.1

854   Inanobe, A., & Kurachi, Y. (2014). Membrane channels as integrators of G-protein-mediated signaling.
855   *Biochimica et Biophysica Acta (BBA) - Biomembranes*, *1838*(2), 521–531.
856   https://doi.org/10.1016/j.bbamem.2013.08.018

857   Isaacson, J. S., Solis, J. M., & Nicoll, R. A. (1993). Local and diffuse synaptic actions of GABA in the
858   hippocampus. *Neuron*, *10*(2), 165–175. https://doi.org/10.1016/0896-6273(93)90308-E

859   Jackson, J., Karnani, M. M., Zemelman, B. V., Burdakov, D., & Lee, A. K. (2018). Inhibitory Control of
860   Prefrontal Cortex by the Claustrum. *Neuron*, *99*(5), 1029–1039.e4.
861   https://doi.org/10.1016/j.neuron.2018.07.031

862   Jadi, M., Polsky, A., Schiller, J., & Mel, B. W. (2012). Location-Dependent Effects of Inhibition on Local
863   Spiking in Pyramidal Neuron Dendrites. *PLoS Computational Biology*, *8*(6), e1002550.
864   https://doi.org/10.1371/journal.pcbi.1002550

865   Jang, H. J., Chung, H., Rowland, J. M., Richards, B. A., Kohl, M. M., & Kwag, J. (2020). Distinct roles of
866   parvalbumin and somatostatin interneurons in gating the synchronization of spike times in the
867   neocortex. *Science Advances*, *6*(17), eaay5333. https://doi.org/10.1126/sciadv.aay5333

868   Jia, H., Rochefort, N. L., Chen, X., & Konnerth, A. (2011). In vivo two-photon imaging of sensory-
869   evoked dendritic calcium signals in cortical neurons. *Nature Protocols*, *6*(1), 28–35.
870   https://doi.org/10.1038/nprot.2010.169

871   Jiang, X., Shen, S., Cadwell, C. R., Berens, P., Sinz, F., Ecker, A. S., … Tolias, A. S. (2015). Principles of
872   connectivity among morphologically defined cell types in adult neocortex. *Science (New York,*
873   *N.Y.)*, *350*(6264), aac9462. https://doi.org/10.1126/science.aac9462

874   Kalmbach, B. E., Buchin, A., Long, B., Close, J., Nandi, A., Miller, J. A., … Ting, J. T. (2018). h-Channels
875   Contribute to Divergent Intrinsic Membrane Properties of Supragranular Pyramidal Neurons in
876   Human versus Mouse Cerebral Cortex. *Neuron*, *100*(5), 1194–1208.e5.
877   https://doi.org/10.1016/j.neuron.2018.10.012

Kang Li. (2008). The image stabilizer plugin for ImageJ. Retrieved from http://www.cs.cmu.edu/~kangli/code/Image_Stabilizer.html

Karayannis, T., Elfant, D., Huerta-Ocampo, I., Teki, S., Scott, R. S., Rusakov, D. A., … Capogna, M. (2010). Slow GABA Transient and Receptor Desensitization Shape Synaptic Responses Evoked by Hippocampal Neurogliaform Cells. *Journal of Neuroscience*, *30*(29), 9898–9909. https://doi.org/10.1523/JNEUROSCI.5883-09.2010

Karnani, M. M., Agetsuma, M., & Yuste, R. (2014). A blanket of inhibition: functional inferences from dense inhibitory connectivity. *Current Opinion in Neurobiology*, *26*, 96–102. https://doi.org/10.1016/j.conb.2013.12.015

Karnani, M. M., Jackson, J., Ayzenshtat, I., Tucciarone, J., Manoocheri, K., Snider, W. G., & Yuste, R. (2016). Cooperative Subnetworks of Molecularly Similar Interneurons in Mouse Neocortex. *Neuron*, *90*(1), 86–100. https://doi.org/10.1016/j.neuron.2016.02.037

Kerr, R. A., Bartol, T. M., Kaminsky, B., Dittrich, M., Chang, J.-C. J., Baden, S. B., … Stiles, J. R. (2008). Fast Monte Carlo Simulation Methods for Biological Reaction-Diffusion Systems in Solution and on Surfaces. *SIAM Journal on Scientific Computing*, *30*(6), 3126–3149. https://doi.org/10.1137/070692017

Kirkpatrick, S., Gelatt, C. D., & Vecchi, M. P. (1983). Optimization by Simulated Annealing. *Science*, *220*(4598), 671–680. https://doi.org/10.1126/science.220.4598.671

Klausberger, T. (2009). GABAergic interneurons targeting dendrites of pyramidal cells in the CA1 area of the hippocampus. *European Journal of Neuroscience*, *30*(6), 947–957. https://doi.org/10.1111/j.1460-9568.2009.06913.x

Klausberger, T., & Somogyi, P. (2008). Neuronal Diversity and Temporal Dynamics: The Unity of Hippocampal Circuit Operations. *Science*, *321*(5885), 53–57. https://doi.org/10.1126/science.1149381

Koch, C., Poggio, T., & Torre, V. (1983). Nonlinear interactions in a dendritic tree: localization, timing, and role in information processing. *Proceedings of the National Academy of Sciences*, *80*(9), 2799–2802. https://doi.org/10.1073/pnas.80.9.2799

Korogod, N., Petersen, C. C. H., & Knott, G. W. (2015). Ultrastructural analysis of adult mouse neocortex comparing aldehyde perfusion with cryo fixation. *ELife*, *4*(AUGUST2015), 1–10. https://doi.org/10.7554/eLife.05793

Kulik, A. (2006). Compartment-Dependent Colocalization of Kir3.2-Containing K+ Channels and GABAB Receptors in Hippocampal Pyramidal Cells. *Journal of Neuroscience*, *26*(16), 4289–4297. https://doi.org/10.1523/JNEUROSCI.4178-05.2006

Kulik, Á., Vida, I., Fukazawa, Y., Guetg, N., Kasugai, Y., Marker, C. L., … Shigemoto, R. (2006). Compartment-dependent colocalization of Kir3.2-containing K+ channels and GABAB receptors in hippocampal pyramidal cells. *Journal of Neuroscience*, *26*(16), 4289–4297. https://doi.org/10.1523/JNEUROSCI.4178-05.2006

Kvitsiani, D., Ranade, S., Hangya, B., Taniguchi, H., Huang, J. Z., & Kepecs, A. (2013). Distinct behavioural and network correlates of two interneuron types in prefrontal cortex. *Nature*, *498*(7454), 363–366. https://doi.org/10.1038/nature12176

Larkum, M. E., Kaiser, K. M. M., & Sakmann, B. (2002). Calcium electrogenesis in distal apical dendrites of layer 5 pyramidal cells at a critical frequency of back-propagating action potentials. *Proceedings of the National Academy of Sciences*, *96*(25), 14600–14604. https://doi.org/10.1073/pnas.96.25.14600

922   London, M., & Häusser, M. (2005). Dendritic computation. *Annual Review of Neuroscience*, *28*(1),
923   503–532. https://doi.org/10.1146/annurev.neuro.28.061604.135703

924   Longsworth, L. G. (1952). Diffusion Measurements, at 1°, of Aqueous Solutions of Amino Acids,
925   Peptides and Sugars. *L Journal of the American Chemical Society*, *649*(1950), 1–2.
926   https://doi.org/10.1021/ja01136a059

927   Lörincz, A., Notomi, T., Tamás, G., Shigemoto, R., & Nusser, Z. (2002). Polarized and compartment-
928   dependent distribution of HCN1 in pyramidal cell dendrites. *Nature Neuroscience*, *5*(11), 1185–
929   1193. https://doi.org/10.1038/nn962

930   Mańko, M., Bienvenu, T. C. M., Dalezios, Y., & Capogna, M. (2012). Neurogliaform cells of amygdala:
931   a source of slow phasic inhibition in the basolateral complex. *The Journal of Physiology*, *590*(22),
932   5611–5627. https://doi.org/10.1113/jphysiol.2012.236745

933   Markram, H., Muller, E., Ramaswamy, S., Reimann, M. W., Abdellah, M., Sanchez, C. A., …
934   Schürmann, F. (2015). Reconstruction and Simulation of Neocortical Microcircuitry. *Cell*, *163*(2),
935   456–492. https://doi.org/10.1016/j.cell.2015.09.029

936   Markram, H., Toledo-Rodriguez, M., Wang, Y., Gupta, A., Silberberg, G., & Wu, C. (2004).
937   Interneurons of the neocortical inhibitory system. *Nature Reviews Neuroscience*, *5*(10), 793–
938   807. https://doi.org/10.1038/nrn1519

939   McCarren, M., & Alger, B. E. (1985). Use-dependent depression of IPSPs in rat hippocampal pyramidal
940   cells in vitro. *Journal of Neurophysiology*, *53*(2), 557–571.
941   https://doi.org/10.1152/jn.1985.53.2.557

942   Melone, M., Ciappelloni, S., & Conti, F. (2015). A quantitative analysis of cellular and synaptic
943   localization of GAT-1 and GAT-3 in rat neocortex. *Brain Structure and Function*, *220*(2), 885–897.
944   https://doi.org/10.1007/s00429-013-0690-8

945   Mody, I., De Koninck, Y., Otis, T. S., & Soltesz, I. (1994). Bridging the cleft at GABA synapses in the
946   brain. *Trends in Neurosciences*, *17*(12), 517–525. https://doi.org/10.1016/0166-2236(94)90155-
947   4

948   Müller, C., Beck, H., Coulter, D., & Remy, S. (2012). Inhibitory Control of Linear and Supralinear
949   Dendritic Excitation in CA1 Pyramidal Neurons. *Neuron*, *75*(5), 851–864.
950   https://doi.org/10.1016/j.neuron.2012.06.025

951   Oláh, S., Füle, M., Komlósi, G., Varga, C., Báldi, R., Barzó, P., & Tamás, G. (2009). Regulation of cortical
952   microcircuits by unitary GABA-mediated volume transmission. *Nature*, *461*(7268), 1278–1281.
953   https://doi.org/10.1038/nature08503

954   Overstreet-Wadiche, L., & McBain, C. J. (2015). Neurogliaform cells in cortical circuits. *Nature
955   Reviews Neuroscience*, *16*(8), 458–468. https://doi.org/10.1038/nrn3969

956   Overstreet, L. S., Jones, M. V, & Westbrook, G. L. (2000). Slow desensitization regulates the
957   availability of synaptic GABA(A) receptors. *The Journal of Neuroscience : The Official Journal of
958   the Society for Neuroscience*, *20*(21), 7914–7921. https://doi.org/20/21/7914 [pii]

959   Padgett, C. L., & Slesinger, P. A. (2010). GABAB Receptor Coupling to G-proteins and Ion Channels. In
960   *Advances in Pharmacology* (Vol. 58, pp. 123–147). https://doi.org/10.1016/S1054-
961   3589(10)58006-2

962   Pallotto, M., Watkins, P. V., Fubara, B., Singer, J. H., & Briggman, K. L. (2015). Extracellular space
963   preservation aids the connectomic analysis of neural circuits. *ELife*, *4*(DECEMBER2015), 1–20.
964   https://doi.org/10.7554/eLife.08206

965　Palmer, L. M., Schulz, J. M., Murphy, S. C., Ledergerber, D., Murayama, M., & Larkum, M. E. (2012).
966　　　　The Cellular Basis of GABAB-Mediated Interhemispheric Inhibition. *Science*, *335*(6071), 989–
967　　　　993. https://doi.org/10.1126/science.1217276

968　Palmer, L., Murayama, M., & Larkum, M. (2012). Inhibitory Regulation of Dendritic Activity in vivo.
969　　　　*Frontiers in Neural Circuits*, *6*(MAY2012), 1–10. https://doi.org/10.3389/fncir.2012.00026

970　Perez, J.-B., Segura, J.-M., Abankwa, D., Piguet, J., Martinez, K. L., & Vogel, H. (2006). Monitoring the
971　　　　Diffusion of Single Heterotrimeric G Proteins in Supported Cell-membrane Sheets Reveals their
972　　　　Partitioning into Microdomains. *Journal of Molecular Biology*, *363*(5), 918–930.
973　　　　https://doi.org/10.1016/j.jmb.2006.08.036

974　Poorthuis, R. B., Muhammad, K., Wang, M., Verhoog, M. B., Junek, S., Wrana, A., … Letzkus, J. J.
975　　　　(2018). Rapid Neuromodulation of Layer 1 Interneurons in Human Neocortex. *Cell Reports*,
976　　　　*23*(4), 951–958. https://doi.org/10.1016/j.celrep.2018.03.111

977　Price, C. J. (2005). Neurogliaform Neurons Form a Novel Inhibitory Network in the Hippocampal CA1
978　　　　Area. *Journal of Neuroscience*, *25*(29), 6775–6786. https://doi.org/10.1523/JNEUROSCI.1135-
979　　　　05.2005

980　Qian, N., & Sejnowski, T. J. (1990). When is an inhibitory synapse effective? *Proceedings of the
981　　　　National Academy of Sciences*, *87*(20), 8145–8149. https://doi.org/10.1073/pnas.87.20.8145

982　Robinson, R. B., & Siegelbaum, S. A. (2003). Hyperpolarization-Activated Cation Currents: From
983　　　　Molecules to Physiological Function. *Annual Review of Physiology*, *65*(1), 453–480.
984　　　　https://doi.org/10.1146/annurev.physiol.65.092101.142734

985　Rózsa, M., Baka, J., Bordé, S., Rózsa, B., Katona, G., & Tamás, G. (2017). Unitary GABAergic volume
986　　　　transmission from individual interneurons to astrocytes in the cerebral cortex. *Brain Structure
987　　　　and Function*, *222*(1), 651–659. https://doi.org/10.1007/s00429-015-1166-9

988　Scanziani, M. (2000). GABA Spillover Activates Postsynaptic GABAB Receptors to Control Rhythmic
989　　　　Hippocampal Activity. *Neuron*, *25*(3), 673–681. https://doi.org/10.1016/S0896-6273(00)81069-
990　　　　7

991　Schneider, C. A., Rasband, W. S., & Eliceiri, K. W. (2012). NIH Image to ImageJ: 25 years of image
992　　　　analysis. *Nature Methods*, *9*(7), 671–675. https://doi.org/10.1038/nmeth.2089

993　Schuman, B., Machold, R. P., Hashikawa, Y., Fuzik, J., Fishell, G. J., & Rudy, B. (2019). Four Unique
994　　　　Interneuron Populations Reside in Neocortical Layer 1. *The Journal of Neuroscience*, *39*(1), 125–
995　　　　139. https://doi.org/10.1523/JNEUROSCI.1613-18.2018

996　Sheets, P. L., Suter, B. A., Kiritani, T., Chan, C. S., Surmeier, D. J., & Shepherd, G. M. G. (2011).
997　　　　Corticospinal-specific HCN expression in mouse motor cortex: I h -dependent synaptic
998　　　　integration as a candidate microcircuit mechanism involved in motor control. *Journal of
999　　　　Neurophysiology*, *106*(5), 2216–2231. https://doi.org/10.1152/jn.00232.2011

1000　Silver, R. A. (2003). Estimation of nonuniform quantal parameters with multiple-probability
1001　　　　fluctuation analysis: theory, application and limitations. *Journal of Neuroscience Methods*,
1002　　　　*130*(2), 127–141. https://doi.org/10.1016/j.jneumeth.2003.09.030

1003　Silver, R. A. (2010). Neuronal arithmetic. *Nature Reviews Neuroscience*, *11*(7), 474–489.
1004　　　　https://doi.org/10.1038/nrn2864

1005　Simon, A., Oláh, S., Molnár, G., Szabadics, J., & Tamás, G. (2005). Gap-Junctional Coupling between
1006　　　　Neurogliaform Cells and Various Interneuron Types in the Neocortex. *Journal of Neuroscience*,
1007　　　　*25*(27), 6278–6285. https://doi.org/10.1523/jneurosci.1431-05.2005

1008   Sodickson, D. L., & Bean, B. P. (1996). GABA B Receptor-Activated Inwardly Rectifying Potassium
1009   Current in Dissociated Hippocampal CA3 Neurons. *The Journal of Neuroscience*, *16*(20), 6374–
1010   6385. https://doi.org/10.1523/JNEUROSCI.16-20-06374.1996

1011   Staley, K. J., & Proctor, W. R. (1999). Modulation of mammalian dendritic GABA A receptor function
1012   by the kinetics of Cl − and HCO 3 − transport. *The Journal of Physiology*, *519*(3), 693–712.
1013   https://doi.org/10.1111/j.1469-7793.1999.0693n.x

1014   Stanfield, P. R., Nakajima, S., & Nakajima, Y. (2002). Constitutively active and G-protein coupled
1015   inward rectifier K+ channels: Kir2.0 and Kir3.0. *Reviews of Physiology Biochemistry and*
1016   *Pharmacology, Vol 145*, *145*, 47–179.

1017   Sykova, E., & Nicholson, C. (2008). Diffusion in Brain Extracellular Space. *Physiological Reviews*, *88*(4),
1018   1277–1340. https://doi.org/10.1152/physrev.00027.2007

1019   Szabadics, J., Tamas, G., & Soltesz, I. (2007). Different transmitter transients underlie presynaptic cell
1020   type specificity of GABAA,slow and GABAA,fast. *Proc Natl Acad Sci U S A*, *104*(37), 14831–
1021   14836.

1022   Tamas, G. (2003). Identified Sources and Targets of Slow Inhibition in the Neocortex. *Science*,
1023   *299*(5614), 1902–1905. https://doi.org/10.1126/science.1082053

1024   Tamás, G., Simon Anna, A. L., & Szabadics, J. (2003). Identified Sources and Targets of Slow Inhibition
1025   in the Neocortex. *Science*, *299*(5614), 1902 LP-1905.

1026   Tamás, G., Szabadics, J., & Somogyi, P. (2002). Cell Type- and Subcellular Position-Dependent
1027   Summation of Unitary Postsynaptic Potentials in Neocortical Neurons. *The Journal of*
1028   *Neuroscience*, *22*(3), 740–747. https://doi.org/10.1523/JNEUROSCI.22-03-00740.2002

1029   Tao, A., Tao, L., & Nicholson, C. (2005). Cell cavities increase tortuosity in brain extracellular space.
1030   *Journal of Theoretical Biology*, *234*(4), 525–536. https://doi.org/10.1016/j.jtbi.2004.12.009

1031   Terunuma, M. (2018). Diversity of structure and function of GABAB receptors: a complexity of
1032   GABAB-mediated signaling. *Proceedings of the Japan Academy, Series B*, *94*(10), 390–411.
1033   https://doi.org/10.2183/pjab.94.026

1034   Thomson, A. ., & Destexhe, A. (1999). Dual intracellular recordings and computational models of slow
1035   inhibitory postsynaptic potentials in rat neocortical and hippocampal slices. *Neuroscience*,
1036   *92*(4), 1193–1215. https://doi.org/10.1016/S0306-4522(99)00021-4

1037   Uematsu, M., Hirai, Y., Karube, F., Ebihara, S., Kato, M., Abe, K., … Kawaguchi, Y. (2008). Quantitative
1038   Chemical Composition of Cortical GABAergic Neurons Revealed in Transgenic Venus-Expressing
1039   Rats. *Cerebral Cortex*, *18*(2), 315–330. https://doi.org/10.1093/cercor/bhm056

1040   Velimirovic, B. M., Gordon, E. A., Nancy F Lim, B. N., & Clapham, D. E. (1996). The K+channel inward
1041   rectifier subunits form a channel similar to neuronal G protein-gated K+channel. *FEBS Letters*,
1042   *379*(1), 31–37. https://doi.org/10.1016/0014-5793(95)01465-9

1043   Vida, I., Halasy, K., Szinyei, C., Somogyi, P., & Buhl, E. H. (1998). Unitary IPSPs evoked by interneurons
1044   at the stratum radiatum-stratum lacunosum-moleculare border in the CA1 area of the rat
1045   hippocampus in vitro. *Journal of Physiology*, *506*(3), 755–773. https://doi.org/10.1111/j.1469-
1046   7793.1998.755bv.x

1047   Wang, W., Touhara, K. K., Weir, K., Bean, B. P., & MacKinnon, R. (2016). Cooperative regulation by G
1048   proteins and Na+ of neuronal GIRK2 K+ channels. *ELife*, *5*. https://doi.org/10.7554/elife.15751

1049   Wickman, K., & Clapham, D. E. (1995). Ion channel regulation by G proteins. *Physiological Reviews*,
1050   *75*(4), 865–885. https://doi.org/10.1152/physrev.1995.75.4.865

1051   Wozny, C., & Williams, S. R. (2011). Specificity of Synaptic Connectivity between Layer 1 Inhibitory
1052   Interneurons and Layer 2/3 Pyramidal Neurons in the Rat Neocortex. *Cerebral Cortex*, *21*(8),
1053   1818–1826. https://doi.org/10.1093/cercor/bhq257

1054   Yakubovich, D., Berlin, S., Kahanovitch, U., Rubinstein, M., Farhy-Tselnicker, I., Styr, B., … Dascal, N.
1055   (2015). A Quantitative Model of the GIRK1/2 Channel Reveals That Its Basal and Evoked
1056   Activities Are Controlled by Unequal Stoichiometry of Gα and Gβγ. *PLOS Computational Biology*,
1057   *11*(11), e1004598. https://doi.org/10.1371/journal.pcbi.1004598

1058   Yao, X. H., Wang, M., He, X. N., He, F., Zhang, S. Q., Lu, W., … Yu, Y. C. (2016). Electrical coupling
1059   regulates layer 1 interneuron microcircuit formation in the neocortex. *Nature Communications*,
1060   *7*, 1–15. https://doi.org/10.1038/ncomms12229

1061

1062

1063   **Supplementary Information**

1064
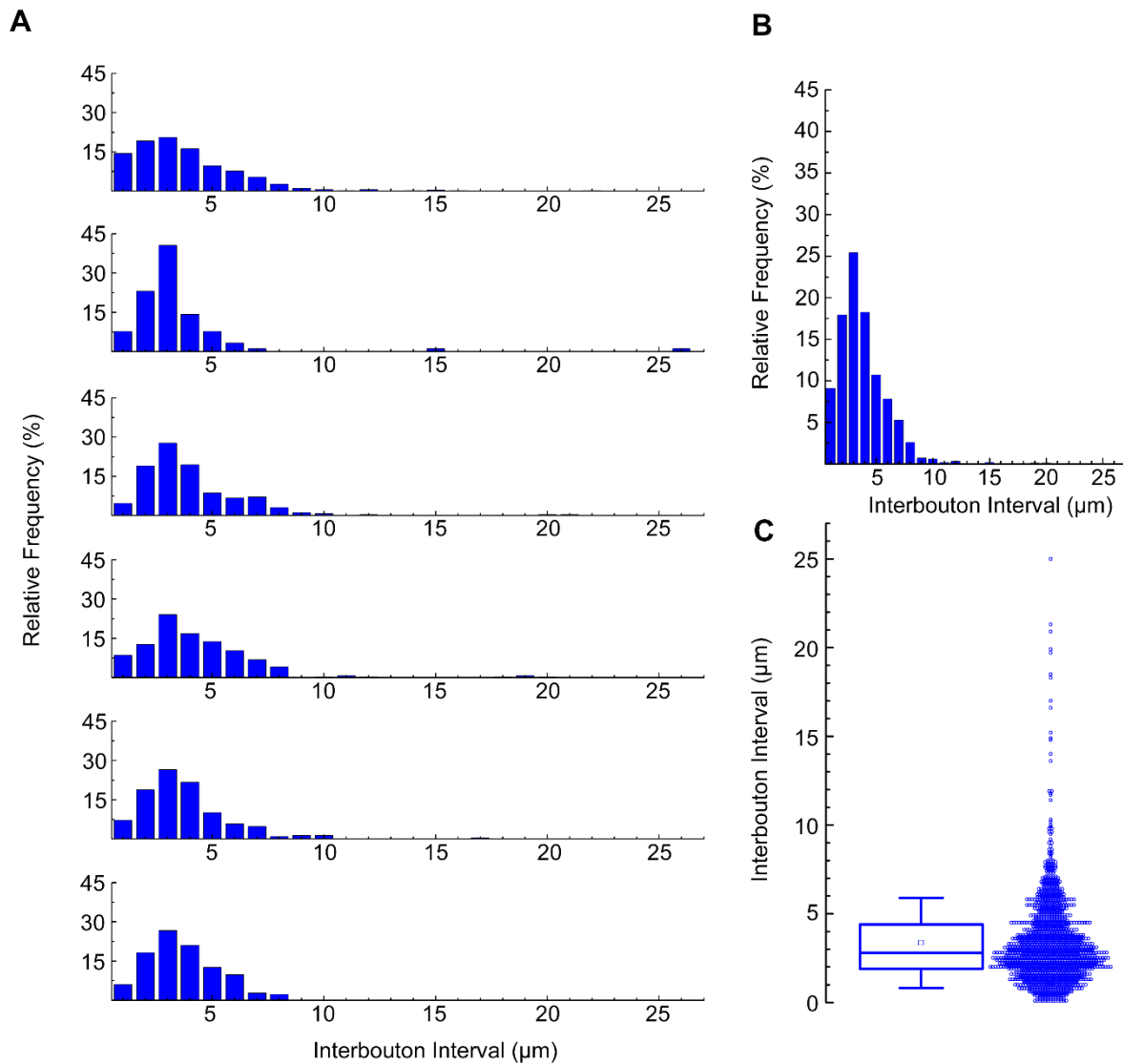
1065

1066   **Sup. Fig 1.- Related to Fig 2. Calculation of NGFC's interbouton interval. (a)** Distribution of interbouton
1067   distances from 6 NGFCs (number of boutons from each morphological analysis were
1068   n=442,91,213,252,291,207). The axonal segments were randomly selected (bin size = 1μm). **(b)**
1069   Average distribution of interbouton intervals in all NGFCs (bin size = 1μm). **(c)** Boxplot shows the
1070   mean±SD (3.357±2.535; n=1495) of all NGFCs' interbouton interval.
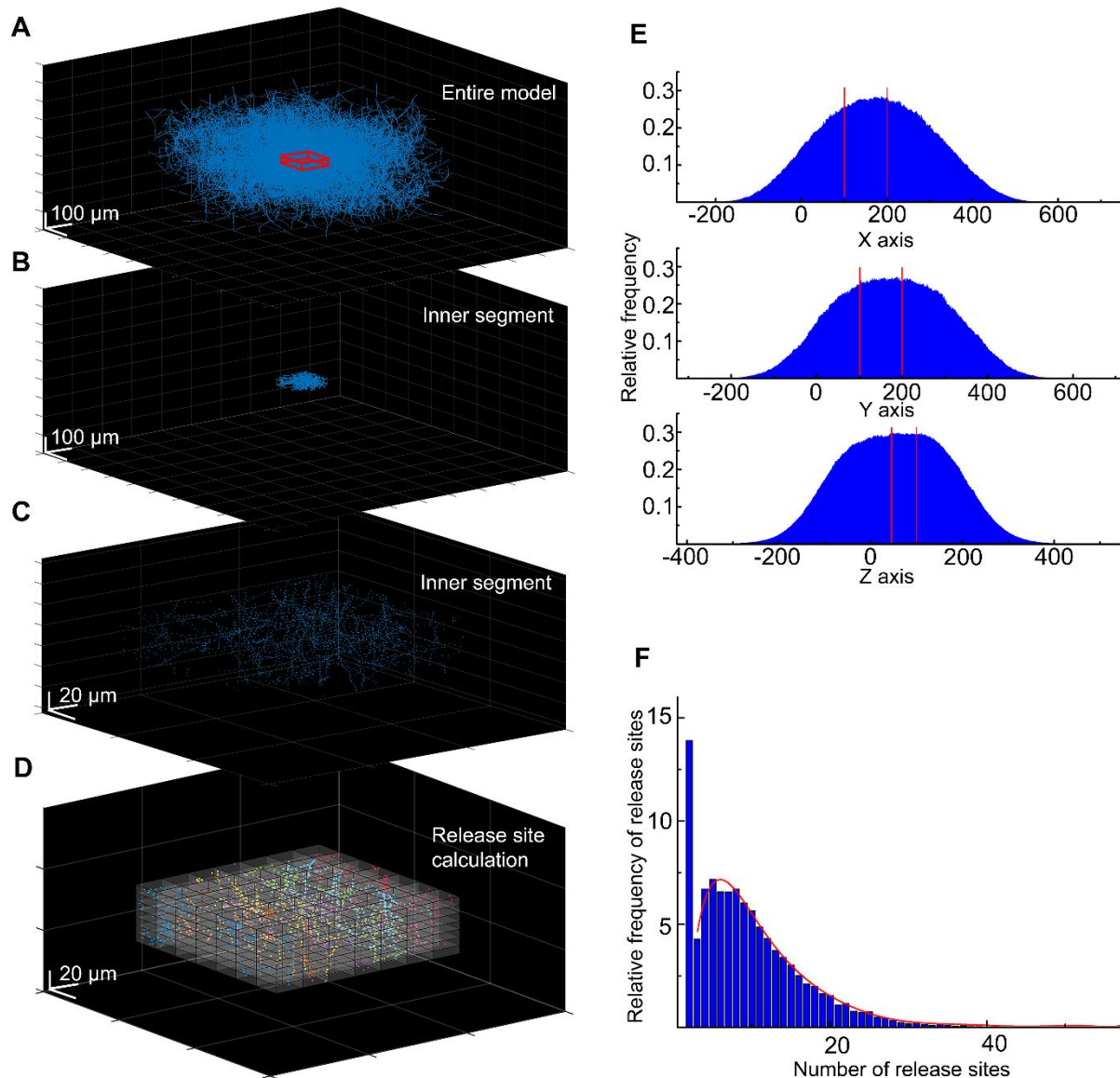
1071

Sup. Fig. 2- Related to Fig 6. Calculation of the NGFC release site density for the MCell model. (**a**) In the spatial model of the NGFC population, the density of axonal processes and release sites are rapidly declining around the model's outskirts. To avoid underrepresentation of release sites, we collected data from the inner section of the model, from a 100x100x50 μm sized cuboid (showed in red). (**b**) Within these boundaries (the section between the two red lines) the high density of release sites is preserved alongside all three axes. (**c**) In the inner segment of the model, we calculated the frequency of release sites in smaller 13.28x13.28x3.592 μm sized cuboids. (**d**) We calculated the release site frequency within the inner segments in all (n=36) simulations in 13.28x13.28x3.592 μm volumes. (**e**) In each simulation, on average 2611.5±691.96 and a total of 94014 release sites were calculated. (**f**) Data shows that 13.9% of segmented volumes do not contain release sites. In 86.1% of segmented volumes, the release site frequency shows a skewed distribution from 1 to 56 (mean:7.61±6.71). The red line shows the fitting of this data.
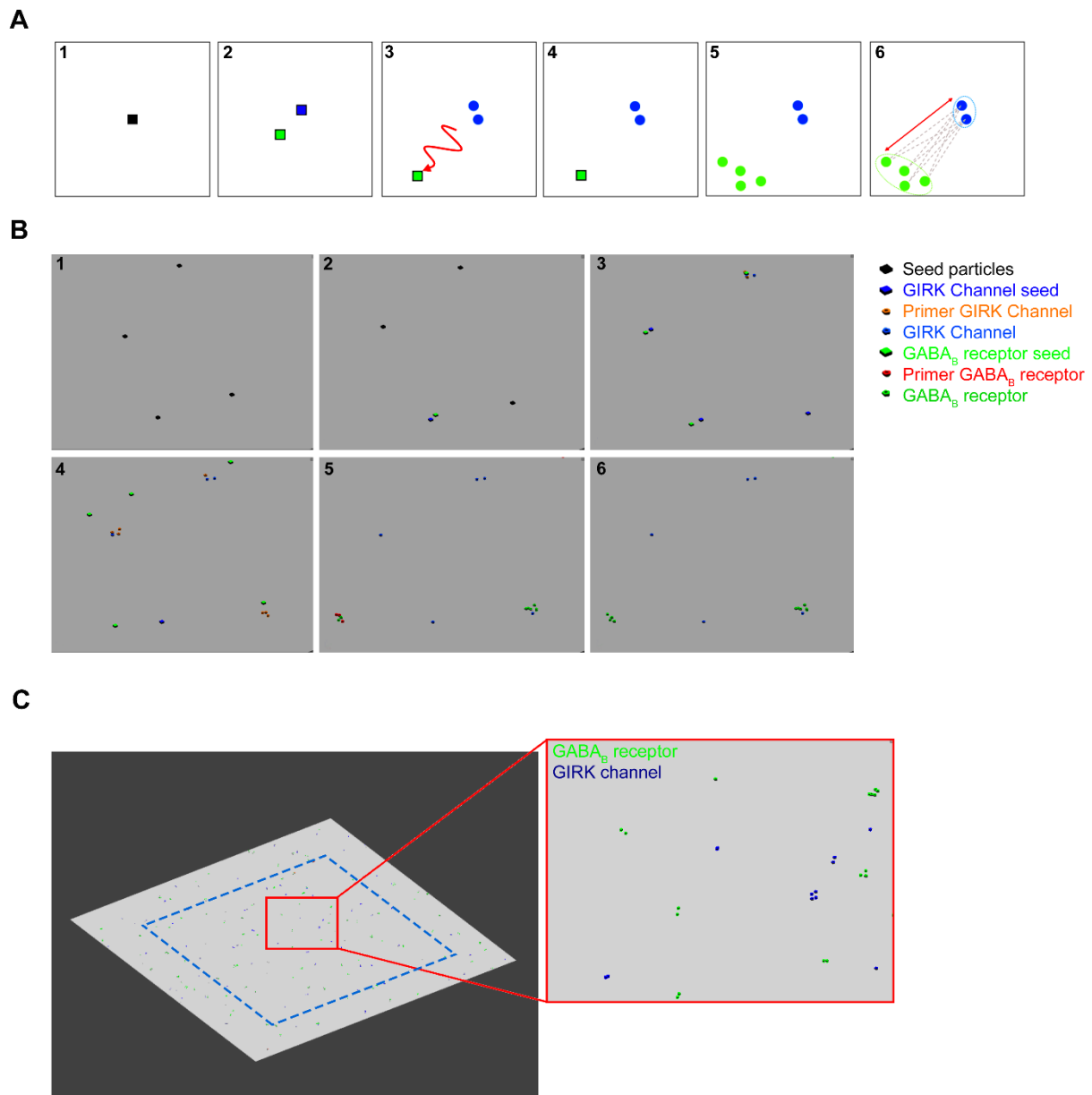
1084

Sup. Fig. 3. GABA$_B$ receptor and GIRK channel distribution, created by a cascade reaction. (a) To create a pseudorandom distribution the molecular interactions the following steps were defined as the schematic concept: (1) Seed particles (black square) were placed randomly along the membrane surface. (2) The seed particles produce two distinctive particles: the first particle, the GIRK channel seed (blue square) that immediately creates GIRK channels (blue circles) and it remains immobile. (4) The second particle is the GABA$_B$ receptor seed (green square), which has the ability to laterally diffuse. (5) The probabilistic distance between the static GIRK channels and the GABA$_B$ receptor seed can be adjusted by limiting the time while it is mobile. After became immobile, the GABA$_B$ receptor seed produces GABA$_B$ receptors. (6) The distance between each GIRK channel and the nearest GABA$_B$ receptors was calculated. (**b**) Image sequences show the particle interactions in the MCell model: (1) Primer seed particles were placed randomly, (2) which produce GIRK channel seed and GABA$_B$ receptor seed particles. (3) GIRK channel seed particles remain in the same place, the GABA$_B$ receptor seed particles laterally diffuse away. (4) GIRK channel seed particles produce 1 to 4 GIRK channels by first

1098   creating 4 primer GIRK channel particles that either disappear or produce a final GIRK channel. This
1099   step was created to avoid uniform cluster generation. (5) $GABA_B$ receptor seeds lateral diffusion time
1100   was optimized to regulate the probabilistic distance between the cluster. $GABA_B$ receptor seed
1101   generated 1 to 8 $GABA_B$ receptors, that either disappeared or produced a functional receptor. (6)
1102   Finally, distances were measured between the closest receptor and channel cluster. (**c**) Images show
1103   the two-dimensional plane and inset of a zoomed image of the final distribution. Distances were only
1104   measured from the GIRK channels that were inside the blue dashed line.

1105
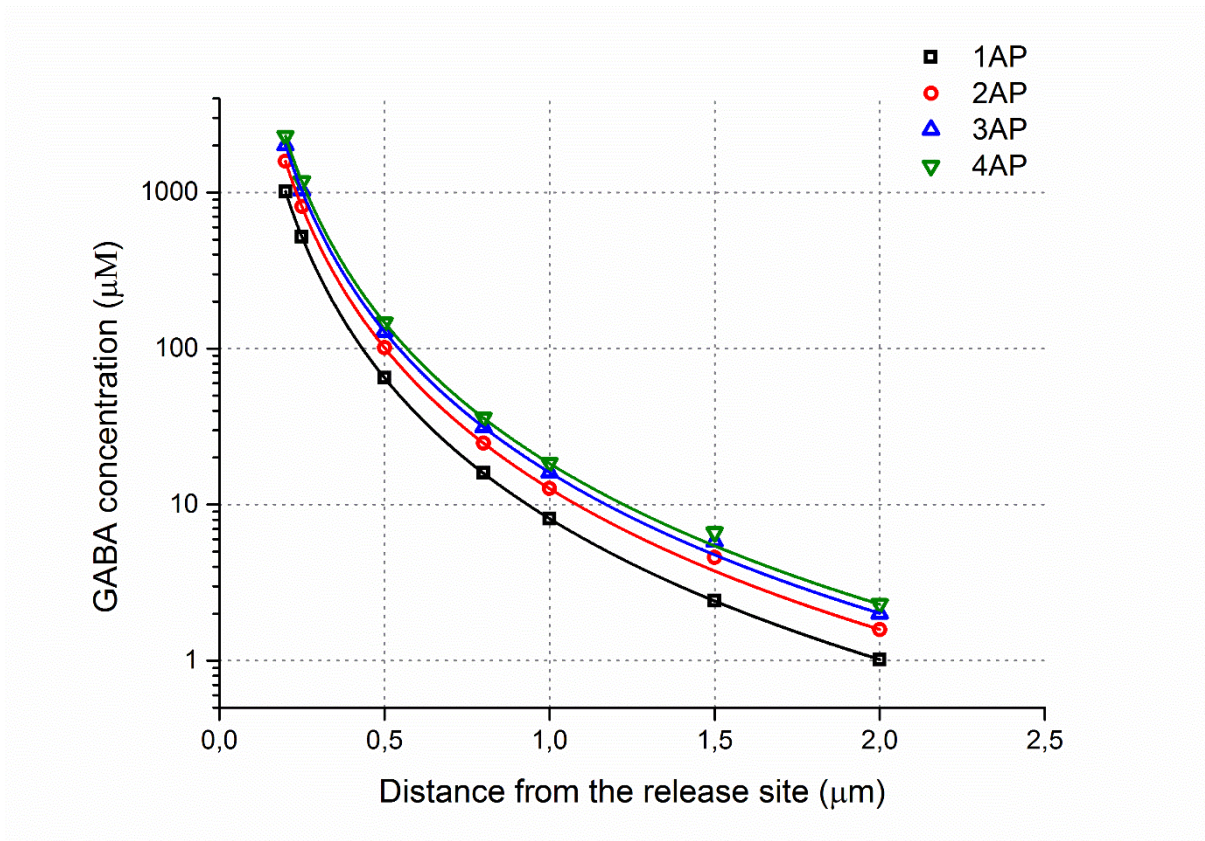
1106

Sup. Fig 4. Estimated GABA spatial concentration profiles during multiple releases. A plot of the GABA concentrations versus distance from the release site in the MCell model.

1107

1108

1109

Distance from the release site (µm)	GABA concentration (µM)			
	1 AP	2AP	3AP	4AP
0.2	1017.06	1584.614	2010.05	2296.08
0.25	520.97	811.56	1029.45	1175.94
0.5	65.022	101.28	128.48	146.76
0.8	15.92	24.8	31.46	35.94
1	8.13	12.67	16.07	18.4
1.5	2.42	4.58	5.81	6.64
2	1.02	1.58	2.01	2.3

1110

1111 **Sup. Table 1. Different estimated GABA concentrations as a function of distance**

1112